Characteristic Critical Collapse with Null Infinity

Rita Pinto Santos

Thesis to obtain the Master of Science Degree in

Engineering Physics

Supervisors: Prof. David Matthew Hilditch
M. Sc. Krinio Marouda

Examination Committee

Chairperson: Prof. Ana Maria Vergueiro Monteiro Cidade Mourão
Supervisor: Prof. David Matthew Hilditch
Members of the Committee: Dr. Alex Vañó Viñuales
Dr. Athanasios Giannakopoulos

November 2023

Not knowing is most intimate.

Declaration

I declare that this document is an original work of my own authorship and that it fulfills all the requirements of the Code of Conduct and Good Practices of the Universidade de Lisboa.

Acknowledgments

I deeply thank my supervisors, David and Krinio. I truly appreciate your support and the wisdom you shared with me. I am sure that the experience I had writing this thesis would be much different if I didn't have you as supervisors.

My brother, I look up to you more than anyone. I am incredibly grateful to have you in my life, as you are a role model to me. Our insightful science discussions are a big part of why I am standing where I am.

I thank my parents for their unconditional support throughout the years. I am certain I can count on you through easy and hard times. At times in which I doubted the road I was walking, you've helped me make my own path, believing in my capabilities more than anyone.

I would have never become who I am today without my grandparents. You have taught me love and dedication. This thesis is a result of you.

I want to thank João Vasconcelos for helping me run experiments on Baltasar and Oolon. Your technical support was crucial for this thesis.

Lastly, I am very grateful to have amazing and inspiring people in my life whom I thank: Maria, Megui, Inês, Mafalda, Mimi, Paulo, David, Ana, Pedro, Valente and Francisco. For the culture shared, the causes advocated, the books exchanged, the rocks climbed, the philosophy discussed; essentially, thank you for *doing life* with me.

I believe you are all part of the person I am. This thesis is also a result of you, through me.

"(...) *todos nascemos filhos de mil pais e mil mães, e a solidão é sobretudo a incapacidade de ver qualquer pessoa como nos pertencendo, para que nos pertença de verdade e se gere um cuidado mútuo. Como se os nossos mil pais e as nossas mil mães coincidissem em parte, como se fôssemos por aí irmãos, irmãos uns dos outros. Somos o resultado de tanta gente, de tanta história, tão grandes sonhos que vão passando de pessoa a pessoa, que nunca estaremos sós.*", Valter Hugo Mãe.

To all of you who will never let me feel alone.

Abstract

Solutions to the Einstein's equations that are close to the threshold of black hole formation exhibit features that resemble critical phenomena in statistical mechanics. In this work, we thoroughly study the critical collapse of a scalar field, focusing both on local and global aspects of such collapse. First, we show that the collapsing field has local Discretely Self-Similar (DSS) behaviour with an echoing period of $\Delta \approx 3.4$. Remarkably, global quantities such as the Bondi mass and News Function manifest the same DSS behaviour. Second, the mass of black holes formed in evolutions near the threshold is shown to scale as a function of the distance to the critical parameter, with a criticality exponent of $\gamma \approx 0.37$. Lastly, we show that these results are universal with respect to the initial data. Our numerical scheme is based on a characteristic formulation in compactified Bondi coordinates, with methods that are globally fourth-order accurate. The convergence of the code is tested, and the accuracy is improved by employing analytical mesh refinement. Finally, the collapse of a Yang-Mills field is studied. We show good convergence for this code, and a preliminary analysis of critical phenomena is provided.

Keywords

General Relativity; Numerical Relativity; Gravitational Collapse; Critical Collapse; Compactification.

Resumo

Soluções das equações de Einstein que estão próximas do limite de formação de buracos negros exibem características que relembram fenómenos críticos em mecânica estatística. Neste trabalho, estudamos detalhadamente o colapso crítico de um campo escalar, focando-nos tanto em aspetos locais como globais. Primeiro, mostramos que o campo que colapsa é discretamente auto-semelhante com um período de eco de $\Delta \approx 3.4$. Notavelmente, quantidades globais como a massa de Bondi ou a função de notícias manifestam o mesmo comportamento discretamente auto-semelhante. Segundo, demonstramos que a massa de buracos negros formados em evoluções perto do limite escala em função da distância ao parâmetro crítico, com um expoente crítico de $\gamma \approx 0.37$. Por último, argumentamos que estes resultados são universais em relação aos dados iniciais. O nosso esquema numérico é baseado numa formulação característica em coordenadas de Bondi compactificadas, com métodos que são globalmente precisos à quarta ordem. A convergência do código é testada e a precisão é melhorada empregando um refinamento analítico da grelha. Finalmente, o colapso de um campo de Yang-Mills é estudado. Este código mostra boa convergência e é fornecida uma análise preliminar do seu colapso crítico.

Palavras Chave

Relatividade Geral; Relatividade Numérica; Colapso Gravitacional; Colapso Crítico; Compactificação.

Contents

1 Introduction 1
1.1 Organization of the Document 4
2 Scientific Background 5
2.1 Critical Collapse 7
2.1.1 Universality 7
2.1.2 Self-Similarity 8
2.1.3 Scaling 9
2.2 Geometric Setup 10
2.2.1 Coordinates 10
2.2.2 Compactification 11
2.3 Analytic Setup 11
2.3.1 Scalar Field Regularity Conditions 12
2.3.2 Scalar Field Collapse Equations 13
2.3.2.A Einstein's Equations 13
2.3.2.B Wave Equation 14
2.3.3 Yang-Mills Field Regularity Conditions 14
2.3.4 Yang-Mills Field Collapse Equations 15
2.3.4.A Einstein's Equations 15
2.3.4.B Wave Equation 16
2.3.5 Asymptotic Quantities 16
2.3.5.A Bondi Mass 16
2.3.5.B News Function 18
2.4 Related Work 18
3 Numerical Methods 21
3.1 Characteristic Initial Value Problem 23
3.2 Scalar Field Evolution Scheme 23
3.3 Yang-Mills Field Evolution Scheme 24

3.4 Finite Differencing . . . 25
3.5 Artificial Dissipation . . . 26
3.6 Truncation Error Matching . . . 27
3.7 Analytic Mesh Refinement . . . 28
3.8 CFL-Stability Condition . . . 29
3.9 Code Validation . . . 30
  3.9.1 Norm Convergence Test . . . 30
  3.9.2 Pointwise Convergence Test . . . 31

4 Preparatory Work **33**
4.1 Toy Model . . . 35
4.2 Convergence Tests . . . 36

5 Numerical Results **39**
5.1 Scalar Field Collapse . . . 41
  5.1.1 Convergence Tests . . . 41
  5.1.2 Initial Data and Diagnostics . . . 44
  5.1.3 Identification of Critical Behaviour . . . 46
  5.1.4 DSS Behaviour in Local and Global Quantities . . . 49
  5.1.5 Black Hole Mass Scaling . . . 51
  5.1.6 Bondi Mass Decay . . . 53
  5.1.7 Universality . . . 54
5.2 Yang-Mills Field Collapse . . . 55
  5.2.1 Yang-Mills Toy Models . . . 57
  5.2.2 Convergence Tests . . . 59
  5.2.3 Identification of Critical Behaviour . . . 59
  5.2.4 Bondi Mass Decay . . . 61
  5.2.5 Preliminary Study of DSS Behaviour in Local Quantities . . . 62

6 Conclusions **65**
6.1 Conclusions . . . 67
6.2 Future Work . . . 68

Bibliography **69**

A DSS Behaviour Results **71**

List of Figures

2.1 Phase space of near-critical evolutions. Reproduced from [1]. 8

2.2 Bondi coordinates in spherical symmetry. Reproduced from [1]. 11

4.1 Given data for f and g evolution. 36

4.2 Pointwise convergence plots for f and g at last timestep of evolution. 37

4.3 Convergence factor Q(t) throughout the evolution. On the left, we show each evolution variable individually, and on the right we show the norm of all variables together. 37

5.1 Convergence factor Q(t) throughout the evolution for a uniform grid, using a code that is globally second-order accurate. The dotted lines correspond to the result obtained with a grid with 100 points and the solid lines correspond to a grid with 200 points. On the left, we show Q(t) for each evolution variable individually, and on the right we show the norm of all the variables together. An initial pulse of amplitude $A = 0.1$ was considered. 42

5.2 Convergence factor Q(t) throughout the evolution for a uniform grid, using a code that is globally fourth-order accurate. The dotted lines correspond to a grid with 100 points and the solid lines correspond to a grid with 200 points. On the left, we show Q(t) for each evolution variable individually, and on the right we show the norm of all the variables together. An initial pulse of amplitude $A = 0.1$ is considered. 42

5.3 Pointwise convergence for each evolution variable. The values presented are computed using a uniform grid, in code that is globally second-order accurate. The timestep presented corresponds to $t = 0.5$. The orange curves are rescaled by a factor of 2^4 (see Section 3.9). 43

5.4 Pointwise convergence for each evolution variable. The values presented are computed using a uniform grid, in code that is globally fourth-order accurate. The timestep presented corresponds to $t = 0.5$. The orange curves are rescaled by a factor of 2^4 (see Section 3.9). 44

5.5 Convergence factor Q(t) throughout the evolution for an unevenly spaced grid in x. The dotted lines correspond to a grid with 200 points and the solid lines correspond to a grid with 400 points. On the left, we show Q(t) for each evolution variable individually, and on the right we show the norm of all the variables together. An initial pulse of amplitude $A = 0.01$ is considered. 45

5.6 Convergence factor Q(t) throughout the evolution for an unevenly spaced grid in x. The dotted lines correspond to a grid with 100 points and the solid lines correspond to a grid with 200 points. On the left, we show Q(t) for each evolution variable individually, and on the right we show the norm of all the variables together. An initial pulse of amplitude $A = 0.01$ is considered. 45

5.7 Scalar field ψ throughout the evolution. On the left, we plot a subcritical evolution with an initial $A = 0.01$ and on the right we plot a supercritical evolution with $A = 0.15$. 48

5.8 Misner-Sharp mass m throughout the evolution. On the left, we plot a subcritical evolution with an initial $A = 0.01$ and on the right we plot a supercritical evolution with $A = 0.15$. . . 48

5.9 Scalar field at the origin as a function of proper time u and adapted time T for a run of N=2×10^5 and global fourth-order accuracy, tuned to 10 decimal places, with $A = 0.12465050165997141$. 49

5.10 News function at future null infinity as a function of Bondi time u_B and adapted time T. The data here presented corresponds to the same run as Figure 5.9. 50

5.11 Bondi mass as a function of Bondi time u_B and adapted time T. The data here presented corresponds to the same run as Figure 5.9. The vertical lines displayed have a separation of $\Delta/2 = 3.43114040/2$. 50

5.12 Redshift $H = \beta(u_C, \infty)$ for a near supercritical evolution as a function of similarity time T. The data shown corresponds to a run with 2×10^5 points, with A=0.12465050166078954 and tuned to 10 decimal places. 51

5.13 Compactness max($\frac{2m}{r}$) for a near-critical evolution as a function of similarity time T. The data shown corresponds to a run with 2000 points, with $A = 0.12465049029170885$ (See Table 5.1). 52

5.14 Final black hole mass as a function of the distance to the critical parameter p^*. The black hole mass is found to scale as $\ln(m_{BH}) = 0.3731 \ln(p - p*) - 0.7353$. Following from this relation we find a critical exponent of $\gamma = \frac{0.7462}{2} \approx 0.3731$. Each point in this figure corresponds to the final black hole mass of an evolution with 2000 gridpoints, performed in a uniform grid. 52

5.15 Comparing Bondi mass decay for initial data that is very subcritical (A=0.001), subcritical (A=0.1256) and supercritical (A=0.17). In the subcritical case, the Bondi mass is found to decay for late times with a power-law exponent of [Pleaseinsertintopreamble]2.43. 54

5.16 We compare the mass loss at future null infinity $\mathscr{I}^+$. The numerical values refer to the values obtained by taking a time derivative of m solved throughout our evolution. The analytical value refers to the values computed using a derived equation for the mass loss at $\mathscr{I}^+$. 54

5.17 Scalar field at the origin as a function of similarity time T and adapted time T. The results shown correspond to a run with $\sigma = 0.5$, and $N = 2000$ points in a uniform grid, tuned to 11 decimal places in $A^* = 0.16671677902267223$. Although the initial data in this picture differs from previous sections, we are able to obtain the same critical phenomena picture as before (see Figure 5.9). 56

5.18 Final black hole mass as a function of the distance to the critical parameter p^*. The black hole mass is found to scale as $\ln(m_{BH}) = 0.3765\ln(p - p*) - 0.4414$. Following from this relation we find a critical exponent of $\gamma \approx 0.3765$. Each point in this figure corresponds to the final black hole mass of an evolution with 2000 gridpoints, performed in a uniform grid. 56

5.19 Convergence factor Q(t) throughout the evolution for the first Yang-Mills toy model, using a code that is globally second-order accurate. The dotted lines correspond to a grid with 100 points and the solid lines correspond to a grid with 200 points. On the left, we show Q(t) for each evolution variable individually, and on the right we show the norm of all the variables together. The dotted lines correspond to a grid with 100 points and the solid lines correspond to a grid with 200 points. We can see that as we increase resolution the convergence factor Q gets closer to 2, both for each field individually as for the single norm. An initial pulse of amplitude $A = 0.01$ was considered. 58

5.20 Convergence factor Q(t) throughout the evolution for the second Yang-Mills toy model, using a code that is globally second-order accurate. The dotted lines correspond to a grid with 100 points and the solid lines correspond to a grid with 200 points. On the left, we show Q(t) for each evolution variable individually, and on the right we show the norm of all the variables together. An initial pulse of amplitude $A = 0.01$ was considered. 59

5.21 Convergence factor Q(t) throughout the evolution for a uniform grid, using a code that is globally second-order accurate. The dotted lines correspond to a grid with 100 points and the solid lines correspond to a grid with 200 points. On the left, we show Q(t) for each evolution variable individually, and on the right we show the norm of all the variables together. 60

5.22 $\xi = W - 1$ throughout the evolution. On the left, we plot a subcritical evolution with an initial $A = 0.01$ and on the right we plot a supercritical evolution with $A = 0.092$ for $N = 400$. 60

5.23 Misner-Sharp mass m throughout the evolution. On the left, we plot a subcritical evolution with an initial $A = 0.01$ and on the right we plot a supercritical evolution with $A = 0.092$ for $N = 400$. 61

5.24 We compare the mass loss at future null infinity $\mathscr{I}^+$ for the Yang-Mills collapse code. The numerical values refer to the values obtained by taking a time derivative of m solved throughout our evolution. The analytical value refers to the values computed using a derived equation for the mass loss at $\mathscr{I}^+$. 61

5.25 $\tilde{\chi}$ at the origin as a function of proper time u and adapted time T for a run of N=2000 and global second-order accuracy, tuned to 6 decimal places, with $A = 0.0886421$. 62

A.1 Scalar field at the origin as a function of proper time u and adapted time T for a preliminary run of N=2000 and global second-order accuracy. 73

A.2 Scalar field at the origin as a function of proper time u and adapted time T in a non uniform grid of $N = 1000$ points. The grid parameters used are $\Theta = 0.44$, $n = 4.0$, $k = 0.47$, $m = 0.5$. The critical parameter is $A^* = 0.12491048189863257$, tuned to 10 decimal places. 73

List of Tables

5.1 Critical parameters obtained for the same family of initial data, with different grid setups and code accuracy. All values presented are calculated for evenly spaced grids with different basis resolutions N. A^* denotes the critical amplitude, u^* denotes the accumulation time and Δ is the self similarity echoing period defined in Section 2.1.2. All evolutions are fine-tuned up to 18 decimal places, besides the one with N=2×10^5 which is fine-tuned to 10 decimal places. 47

5.2 Critical parameters obtained for the same family of initial data, with different grid setups and code accuracy. All values presented are calculated for non-uniform grids with different basis resolutions N. The grid parameters in Equation (3.19) are set to $\Theta = 0.44$, $n = 4.0$, $k = 0.47$, $m = 0.5$ in all runs. A^* denotes the critical amplitude, fine tuned up to 10 decimal places, u^* denotes the accumulation time and Δ is the self-similarity echoing period defined in Section 2.1.2. 47

5.3 Critical parameters obtained for different families of initial data, with a uniform grid of 2000 points, using a code that is globally fourth-order accurate. We vary the value of σ and keep $r_0 = 0.7$. A^* denotes the critical amplitude, fine-tuned up to 11 decimal places, u^* denotes the accumulation time and Δ is the self-similarity echoing period defined in Section 2.1.2. 55

Acronyms

ADM	Arnowitt-Deser-Misner
CIVP	Characteristic Initial Value Problem
CSS	Continuous Self-Similar
CFL	Courant-Friedrichs-Levy
DSS	Discretely Self-Similar
EFE	Einstein Field Equations
GR	General Relativity
SSH	Self-Similarity Horizon

1

Introduction

Contents

1.1 Organization of the Document 4

General Relativity (GR) is the most successful gravitation theory, explaining gravity as the curvature of a four dimensional spacetime manifold. This is the essence behind Einstein Field Equations (EFE), a set of non-linear partial differential equations relating the geometry of spacetime with its matter content.

Exact solutions for the EFE can only be found under simplifying assumptions, such as imposing symmetries on the system. One can also use perturbative methods and consider linear perturbations on a background spacetime, obtaining a system of linear differential equations. Alternatively, one can use numerical methods to solve the EFE. This is the essence of the field of Numerical Relativity.

Critical phenomena in gravitational collapse were first discovered by M. Choptuik, who studied the dynamical evolution of one-parameter families of initial data. He found that the evolution of a massless scalar field in spherical symmetry will asymptote to one of two possible end-states: if initial data is dense enough, a black hole will form, or if it is weaker it can disperse to flat spacetime. Moreover, Choptuik found a very interesting characteristic of critical phenomena: just at the threshold of black hole formation the dynamics of the system become relatively simple and universal in some aspects, despite the complicated form of the EFE [2].

Understanding critical collapse is very relevant as critical solutions can be helpful in studying the cosmic censorship conjecture, a long standing problem in GR [3]. Numerical studies of critical collapse allow for the creation of arbitrarily small black holes. Within the exact critical solution, a point with arbitrarily high curvature can be observed from a point with arbitrarily low curvature, which corresponds to the formation of a naked singularity (a singularity with no event horizon). Critical solutions provide counter-examples to some formulations of cosmic censorship which state that naked singularities cannot arise from smooth initial data [3]. By studying critical solutions, we are then testing the validity of the cosmic censorship conjecture.

The first aim of this project is to study the critical collapse of a spherically symmetric scalar field using null coordinates. The code developed is based on a Characteristic Initial Value Problem (CIVP), in which the initial data is specified on a null hypersurface. Our spacetime is then foliated on a family of non-intersecting null hypersurfaces. We compactify our domain in order to include both the origin and $\mathscr{I}^+$ in our computational domain.

Our motivation for this choice of evolution is that it allows us to study the process from the point of view of an observer located at future null infinity $\mathscr{I}^+$, corresponding to the correct idealization of astrophysical observers. Since gravitational radiation is only unambiguously defined at $\mathscr{I}^+$, our choice of numerical setup allows us to study radiation quantities such as the Bondi mass and the News function that can reach gravitational waves detectors. We can also further study numerical methods in this type of spacetime foliation where the parity of fields is non trivial.

Lastly, we begin to study the critical collapse of a Yang-Mills field. While the echoing period in the Discretely Self-Similar (DSS) critical solution for the scalar field is $\Delta \approx 3.44$, with a critical exponent

$\gamma \approx 0.37$, in the Yang-Mills field case we have $\Delta \approx 0.6$ and $\gamma \approx 0.2$ [4]. This means that introducing the Yang-Mills field allows for a less computationally demanding study of critical phenomena in gravitational collapse. To our knowledge, critical solutions of a Yang-Mills field collapse haven't been studied in a characteristic approach with a compactified domain.

1.1 Organization of the Document

The following chapter (Chapter 2) provides some additional background information required to understand the rest of the document. We discuss previous works in gravitational collapse, particularly in the case of a scalar field and Yang-Mills field. We compare these works to our approach, exploring how our contributions differ from previous ones. Chapter 3 presents our methodology, discussing the setup chosen for the gravitational collapse study, as well as presenting the concrete physical setup and how we tackle it. Necessary numerical methods and code validation techniques are also discussed. Chapter 4 presents the implementation of a toy model which consists of a simpler implementation of our physical models. Chapter 5 presents the numerical results and analysis of the two cases studied: a massless scalar field collapse and a Yang-Mills field collapse. Finally, Chapter 6 summarizes the findings of this work and discusses future research directions.

2

Scientific Background

Contents

2.1 Critical Collapse 7
2.2 Geometric Setup 10
2.3 Analytic Setup 11
2.4 Related Work 18

In this section, the necessary background for the study of critical phenomena in gravitational collapse is provided. Firstly, we go through the main features of the critical collapse; moving on to a description of the geometry of our problem, followed by the derivation of the necessary equations. We finish this section by making some remarks about related works, laying out how this work differs from previous ones.

2.1 Critical Collapse

Gravitational collapse consists in the process by which energy (for instance, matter or electromagnetic waves) contracts under the influence of its own gravitational field. This mechanism is believed to be behind the structure formation of our universe and was first studied by Oppenheimer and Snyder in 1939, some time after the theory of GR was developed [5].

The dynamics of gravitational collapse are described by Einstein's equations. In spherical symmetry, the collapse of a massless scalar field will asymptote to one of two possible end-states: if the initial data is strong enough, i.e., it is above some criticality threshold, it can collapse and form a Schwarzschild black hole, or if it is weaker, it can disperse to flat spacetime. The so-called critical phenomena occurs when attracting and repulsive effects are almost in balance. In this case, we say the initial configuration is in the threshold of black hole formation [1].

Critical phenomena were first discovered by Choptuik [6] in numerical simulations of a spherical scalar field. The phenomena studied by Choptuik has correspondence to Type II phase transitions in statistical mechanics and thus are usually referred to as critical phenomena of Type II. In this work, we are interested in this type of collapse, since it is characteristic of the phenomena we want to study, i.e. massless scalar fields.

At the threshold between black hole formation and dispersion, solutions to the EFE are characterized by features of critical collapse such as:

- Universality;
- Self-similarity;
- Scaling.

2.1.1 Universality

General Relativity can be treated as a dynamical system of infinite dimensions [1]. Initial data sets correspond to a point in phase space. This data set will be evolved using Einstein's equations, as discussed in Section 3. Solution curves of the evolution are represented in Figure 2.1 for the case of a

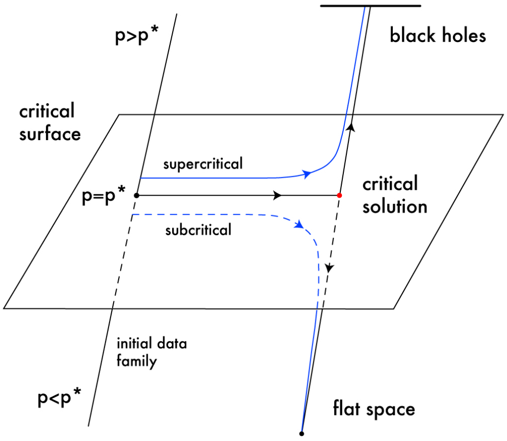

Figure 2.1: Phase space of near-critical evolutions. Reproduced from [1].

scalar field collapse in spherical symmetry. In this scenario, the system ends up either in an end-state of dispersion or formation of a black hole. The two possible end-states of the evolution correspond to basins of attraction in the phase space: Minkowski spacetime is an attractive fixed point and all the possible final black holes form a line segment of attractive fixed points [1].

The phase space is then split in two halves, separated by a critical hypersurface. Initial data that lies precisely on this hypersurface will remain on it throughout the evolution. Thus, the critical hypersurface is itself a dynamical system with one dimension less. The critical solution is an attracting fixed point that lies in the critical hypersurface. This solution is then an attractor of codimension one.

For initial data close to the critical hypersurface, the trajectory defined moves close to the surface for some time. The closer the initial data is to the critical plane, the longer the evolution curve will remain close to the critical plane. In the time the evolution spends in the vicinity of the universal critical solution, all details of the initial data are forgotten, except for the distance from the threshold of black hole formation. That is, all near-critical solutions look the same for a while. This is what is meant by universality of the near-critical behaviour. After some time, as the mode transverse to the surface grows, the curve of evolution drifts away either towards the flat spacetime or black hole end-states.

2.1.2 Self-Similarity

A self-similar solution is a solution which is similar to itself when appropriately scaling the independent and dependent variables. Self-similarity can be observed when initial data is fine-tuned so that its end-state is either a very small black hole or slightly below that, in the scenario of a scalar field collapse in spherical symmetry. That is, carefully chosen initial data will result in a solution curve near the critical plane, which will show self-similarity for some course of the evolution [1]. The more we fine-tune our initial data, the longer this solution will remain close to the critical solution and be self similar, before eventually dispersing.

A spacetime (M, g) is DSS if it admits a discrete diffeomorphism $\Phi_\Delta : M \to M$ which leaves the metric invariant up to a constant scale factor such that

$$(\Phi_\Delta^*)^n \, g|_p = e^{2n\Delta} g|_p, \forall p \in M, \tag{2.1}$$

where $n \in \mathbb{N}$ and Δ is a dimensionless real constant factor [1]. The critical solution discussed in Section 2.1.1 has been found to be DSS, that is, it reproduces itself in echoes. Thus, the critical solution is scale-invariant by a factor of $e^{2n\Delta}$, where Δ is a universal echoing period independent of the initial data. By fine-tuning the initial data, our self-similar solution ϕ will satisfy

$$\phi^*(r, t) = \phi^*(e^{n\Delta} r, e^{n\Delta} t). \tag{2.2}$$

In a similar way, a solution being Continuous Self-Similar (CSS) means that there exists a (generating) vector field $\xi = \frac{d}{d\Delta} \Phi_\Delta|_{\Delta=0}$. Hence, a CSS solution has no period, in opposition to the DSS case we have discussed, in which $\Delta \neq 0$. Thus, ξ obeys the conformal Killing equation with a conventional constant on the right hand side such that

$$\mathcal{L}_\xi g_{\mu\nu} = 2 g_{\mu\nu}. \tag{2.3}$$

Such spacetimes admitting a one-parameter (Δ) family of a diffeomorphism Φ_Δ are said to be CSS. Although in this work we are in fact interested in spacetimes that are DSS, the simpler case of a CSS collapse can sometimes be useful in the study of critical behaviour [7]. There are in fact models that are CSS, as is the case of the critical solution of a spherically symmetric perfect fluid [3].

Finally, we note that Choptuik's critical solution is theoretically DSS throughout the whole evolution, but the critical solutions we'll find in our simulations will only verify self-similarity in a region around the origin, falling off smoothly at null-infinity — just like our initial data. This is consistent with an object sending signals to null-infinity, which is the scenario we want to study [1].

2.1.3 Scaling

An important feature of critical collapse found by Choptuik [6] is related with the mass of the black holes produced near criticality. He found that the mass of the formed black hole depends on a parameter p of a family of initial data and that this relation follows a power-law

$$m_{BH} = k|p - p^*|^\gamma, \tag{2.4}$$

where the constant k and the critical value p^* depend on the particular one-parameter family of initial data — i.e., our scalar field. On the other hand, the critical exponent γ is universal [3].

As in the analysis of Section 2.1.1, the parameter p^* here will dictate the threshold of black hole formation: for a family of initial data with $p > p^*$, a black hole will form, while for $p < p^*$ the initial data is dispersed. The already mentioned interesting behaviour occurs for values of p close to p^*, for which the evolution approaches a universal solution independent of the initial shape of the data, the critical solution.

Note that analogously to the black hole mass case, scaling laws for black hole charge have also been discovered. Black hole angular momentum has also been conjectured to scale in a similar manner [3].

2.2 Geometric Setup

This section provides a description of the geometry of our problem. The choice of coordinates is discussed, as well as their compactification.

2.2.1 Coordinates

In this work, we'll be using coordinates adapted to the null geodesics of spacetime. In fact, we're interested in studying gravitational collapse, which is described by the dynamics of spacetime in a small region around the origin, but using null coordinates will allow us to study the collapse process from the point of view of an observer located at infinity. This observer sees radiation signals emitted by the collapsing field [1].

The general form of a spherically symmetric metric takes the form

$$ds^2 = d\tau^2(t,r) + Y^2(t,r)d\Omega^2(\theta,\phi), \tag{2.5}$$

where $d\tau^2(t,r)$ is a 2D metric of signature (-,+) and $d\Omega^2$ is the metric on the unit 2-sphere. Bondi coordinates are obtained by fixing $x^0 = u$, i.e. u represents a family of outgoing null geodesics. Because we're interested in spherical symmetry, $\{x^2, x^3\} = \{\theta, \phi\}$ are taken to be constant. x^1 is chosen geometrically as $x^1 = r$, such that it's a radial parameter along the null geodesics defined by u. Thus, the line element in Bondi coordinates $\{u, r, \theta, \phi\}$ can be shown to be of the form

$$ds^2 = -e^{2\beta(u,r)}\frac{V(u,r)}{r}du^2 - 2e^{2\beta(u,r)}dudr + r^2(d\theta^2 + sin^2\theta d\phi^2), \tag{2.6}$$

in which $\beta(u,r)$ and $\frac{V(u,r)}{r}$ are smooth metric functions. The physical meaning of these functions is discussed by Pürrer [1]: β is related to the redshift between the centre of symmetry and an asymptotic

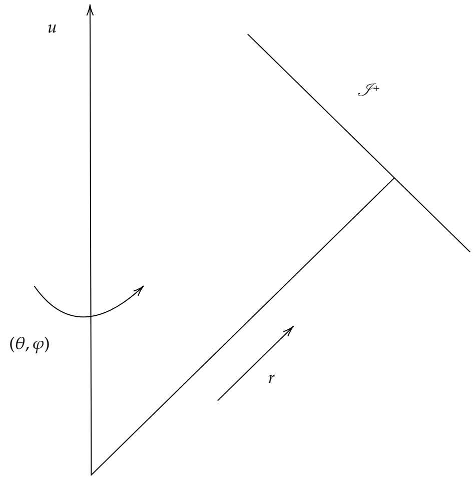

Figure 2.2: Bondi coordinates in spherical symmetry. Reproduced from [1].

observer and V is the analog of a Newtonian potential. Introducing a time coordinate $t = u + r$ in flat space, we can check that the metric based on Bondi coordinates is consistent with the signature (-,+,+,+).

In this work, our gauge choice will be such that our outgoing null slices are parameterized by the proper time of an observer located at the origin, from where the signal is emanating. This simplifies the study of the region close to the centre of spherical symmetry, where critical solutions are DSS, as discussed in Section 2.1.2.

2.2.2 Compactification

In numerical studies of collapsing systems, it is often useful to perform a compactification of the radial coordinate r. We perform a coordinate transformation which maps a half-infinite domain $[0, \infty)$ to a finite one $[0, 1]$, by doing

$$x := \frac{r}{1+r}. \tag{2.7}$$

Points at $\mathscr{I}^+$ are then included in our grid at $x = 1$. In such a manner, we can mimic observers at null-infinity which will allow us to extract global properties of our problem.

2.3 Analytic Setup

In this section, we formulate the equations of the gravitational collapse of a massless scalar field ϕ, as well as of a Yang-Mills field. For both physical scenarios, we discuss the regularity conditions for our fields and metric functions, and then derive the evolution equations.

2.3.1 Scalar Field Regularity Conditions

The regularity of a function at the origin essentially means that there exists a Taylor series expansion around $r = 0$. We also impose local flatness at the centre of spherical symmetry, i.e. the metric goes to the Minkowski metric $\lim_{r\to 0} g_{ab} = \eta_{ab}$. We would like to derive what restrictions these assumptions imply for the metric functions $\beta(r)$ and $V(r)$ that appear in the line element defined in (2.6). We assume an ansatz

$$\begin{aligned} \beta &= a + br + cr^2 + \mathcal{O}(r^3) \\ \frac{V}{r} &= d + er + fr^2 + \mathcal{O}(r^3). \end{aligned} \tag{2.8}$$

This yields

$$\begin{aligned} \beta_{,r} &= b + 2cr + \mathcal{O}(r^2) \\ V_{,r} &= d + 2er + 3fr^2 + \mathcal{O}(r^3). \end{aligned} \tag{2.9}$$

Pürrer, et al. [7] apply this ansatz in the $r \to 0$ limit of the derivatives of the metric. These should remain finite and be independent of the spherical angles θ and ϕ, since these are indefinite at the origin. This provides conditions on the series expansion of β and $\frac{V}{r}$ that yield

$$\begin{aligned} \beta(r) &= \mathcal{O}(r^2) \\ \frac{V(r)}{r} &= 1 + \mathcal{O}(r^2). \end{aligned} \tag{2.10}$$

These are the conditions for the metric to be regular at the centre of spherical symmetry. Thus, in order to obtain a fully regular system of evolution equations, we introduce the Misner-Sharp mass function (2.11). In this way, we eliminate V by using

$$m(u, r) = \frac{r}{2}\left[1 - \frac{V}{r}e^{-2\beta}\right], \tag{2.11}$$

obtaining a regularized set of equations that satisfies (2.10). These conditions are consistent with the hypersurface equation $V_{,r} = e^{2\beta}$ derived in Section 2.3.2.

Let's now investigate the scalar field ϕ. Using the hypersurface equation $\beta_{,r} = 2\pi r(\phi_{,r})^2$ further derived in 2.3.2, then using Equation (2.10) we can see that $\phi_{,x} \to 0$ at the origin. Additionally, from the definition of the Misner-Sharp mass function (2.11) we have $m(r) = \mathcal{O}(r^3)$.

In addition, we can also expand the scalar field around the origin:

$$\phi(r) = \phi_0 + \phi_1 r + \mathcal{O}(r^2) \tag{2.12}$$

and make use of the hypersurface equation $\beta_{,r} = 2\pi r(\phi_{,r})^2$ to see that there are no restrictions on ϕ.

As stated in [1], this happens because the D'Alembertian usually contains terms similar to $\frac{2}{r}\partial_r$ and regularity of the field ϕ at the origin usually amounts to requiring that $\partial_r \phi|_{r=0}$ vanishes. But working with a null coordinate u changes this situation, as this gives rise to an additional term $-\frac{2}{r}\partial_u$ in the D'Alembertian which cancels out the aforementioned term.

2.3.2 Scalar Field Collapse Equations

It is often useful to introduce a rescaled field ψ,

$$\psi = \phi r. \tag{2.13}$$

The amplitude of an outgoing spherical wave packet described by ϕ decreases as $1/r$. Hence, ϕ falls off at large r, but the rescaled field ψ behaves similarly to a plane wave. It is then possible to increase numerical accuracy at large distances, as the amplitude of the plane wave doesn't decrease as fast as in the original case, and should now be $\mathcal{O}(1)$.

2.3.2.A Einstein's Equations

The Einstein Field Equations are given by

$$\begin{aligned} G_{ab} &= 8\pi T_{ab}, \\ T_{ab} &= \nabla_a\phi\nabla_b\phi - \frac{1}{2}g_{ab}\nabla_c\phi\nabla^c\phi, \end{aligned} \tag{2.14}$$

which yields

$$\begin{aligned} T_{ur}(u,r) &= \frac{V\phi_{,r}^2}{2r}, \\ T_{rr}(u,r) &= \phi_{,r}^2. \end{aligned} \tag{2.15}$$

The EFE give two hypersurface equations, one for β and other for V. Making use of the Misner-Sharp mass definition (2.11), these can be written as

$$\begin{aligned} \beta_{,r} &= 2\pi r T_{rr}(u,r), \\ m_{,r} &= 4e^{-2\beta}\pi r^2 T_{ur}(u,r). \end{aligned} \tag{2.16}$$

In the case of a scalar field collapse, the EFE for $\beta(u,r)$ and $V(u,r)$ that will compose our evolution system are then

$$\begin{aligned} \beta_{,r} &= 2\pi r(\phi_{,r})^2, \\ m_{,r} &= (r-2m)\beta_{,r}. \end{aligned} \tag{2.17}$$

These equations are both solved in slices of constant u, thus we refer to them as hypersurface equations.

Using $r = \frac{x}{1-x}$ yields

$$\begin{aligned} \beta_{,x} &= 2\pi x(1-x)\left(\phi_{,x}\right)^2, \\ m_{,x} &= 2\pi x^2\left[1 - \frac{2(1-x)}{x}m\right](\phi_{,x})^2, \end{aligned} \tag{2.18}$$

where $(\phi_{,x})^2 = (\frac{1-x}{x}\psi_{,x} - \frac{\psi}{x^2})^2$. This will be our evolution system for the metric functions.

2.3.2.B Wave Equation

The wave equation for the scalar field ϕ takes the form

$$\Box\phi = \nabla_a \nabla^a \phi = 0, \tag{2.19}$$

in which the curved space d'Alembertian is written in spherical symmetry.

The curved space D'Alembertian operator in curved space can be derived using the formula

$$\Box\phi \equiv \frac{1}{\sqrt{-g}}\partial_a(\sqrt{-g}g^{ab}\partial_b\phi), \tag{2.20}$$

yielding

$$e^{-2\beta}\left[\left(\frac{2V}{r^2} + \left(\frac{V}{r}\right)_{,r}\right)\partial_r - \frac{2}{r}\partial_u - 2\partial_u\partial_r + \frac{V}{r}\partial_{rr}\right]\phi = 0. \tag{2.21}$$

Defining the two dimensional D'Alembertian $\Box_h = e^{-2\beta}\left[\left(\frac{V}{r}\right)_{,r}\partial_r - 2\partial_u\partial_r + \frac{V}{r}\partial_{rr}\right]$ and making use of the rescaled field (2.13) we can rearrange the terms in (2.21) obtaining

$$\Box_h\psi = e^{-2\beta}\left[\left(\frac{V}{r}\right)_{,r}\partial_r - 2\partial_u\partial_r + \frac{V}{r}\partial_{rr}\right]\psi = \left(\frac{V}{r}\right)_{,r}\frac{e^{-2\beta}\psi}{r}. \tag{2.22}$$

Using $V_{,r} = e^{2\beta}$ and the definition of the Misner-Sharp function (which gives $V = e^{2\beta}(r-2m)$), the wave equation (2.22) becomes

$$\left[\frac{1}{r}\partial_r + \frac{1}{r^2}(2m-r)\partial_r - 2e^{-2\beta}\partial_u\partial_r - \frac{2}{r^2}(2m-r)\partial_{rr}\right]\psi = \frac{2m\psi}{r^3}, \tag{2.23}$$

which can can be rewritten as

$$\begin{aligned}\psi_{,ru} =& \frac{e^{2\beta}}{2r^3}\left(-2r^2 m_{,r}\psi_{,r} + 2rm_{,r}\psi - 4r^2 m\beta_{,r}\psi_{,r} - 2r^2 m\psi_{,rr} + 4rm\beta_{,r}\psi\right.\\ &\left.+2rm\psi_{,r} - 2m\psi + 2r^3\beta_{,r}\psi_{,r} + r^3\psi_{,rr} - 2r^2\beta_{,r}\psi\right).\end{aligned} \tag{2.24}$$

In conclusion, our evolution equations consist of the wave equation for the scalar field (Equation (2.24)) and the two hypersurface equations for the metric functions (Equations (2.18)).

2.3.3 Yang-Mills Field Regularity Conditions

We now look for the regularity conditions for the Yang-Mills field W. Following the work of [8] we see that the wave equation for W has a formally singular term associated with the Yang-Mills non-linearity.

In a static spacetime, there are two stable ground state solutions $W = \pm 1$, while the solution $W = 0$ is unstable. We pick the ground state $W = 1$. To avoid the indeterminacy around $r = 0$, we see that the W field has to obey $W = 1 + \mathcal{O}(r^2)$ in this region. Simultaneously, for this term to be regular at $\mathscr{I}^+$ the correct ansatz for W is of the form

$$W = 1 + x^2\chi = 1 + \left(\frac{r}{1+r}\right)^2 \chi, \tag{2.25}$$

in which $\chi(u, r) = \mathcal{O}(1)$ both at the origin and at $\mathscr{I}^+$. To make the numerical implementation more straightforward, we define a new variable $\xi(u, r) \equiv x^2\chi(u, r)$.

2.3.4 Yang-Mills Field Collapse Equations

The purely magnetic Yang-Mills field in spherical symmetry can be parametrised as [4]

$$F = dW \wedge (\tau_1 d\theta + \tau_2 \sin\theta d\phi) - (1 - W^2)\tau_3 d\theta \wedge \sin\theta d\phi, \tag{2.26}$$

where τ_i are the Pauli matrices with $\mathrm{tr}\tau_i\tau_j = \delta_{ij}$.

Similarly to Section 2.3.2, we will derive the wave equations and the EFE in Bondi coordinates, now in the case of the collapse of a Yang-Mills field.

2.3.4.A Einstein's Equations

Following the work of Baumgarte, et al. [4], in the presence of a Yang-Mills field the EFE are

$$G_{ab} = 8\pi T^{(W)}_{ab}, \tag{2.27}$$

with

$$\begin{aligned} T^{(W)}_{ab} &= \tilde{T}^{(W)}_{ab} - \frac{1}{4} g_{ab}\tilde{T}^{(W)}, \\ \tilde{T}^{(W)}_{ab} &= \mathrm{diag}(2r^{-2}\nabla_a W \nabla_b W, P r^2 \gamma_{ab}), \\ P &= r^{-2}\nabla_a W \nabla^a W + r^{-4}(1 - W^2)^2, \end{aligned} \tag{2.28}$$

where $\gamma_{ab} = \mathrm{diag}(1, \sin^2\theta)$ is the unit metric on the 2-sphere and P is a pressure that can be interpreted as the tangential pressure in spherical symmetry. Note that $\tilde{T}^{(W)}_{ab}$ is block diagonal in the uu, ur and rr components, and diagonal in the rest. We use the line element defined by Equation (2.6). The relevant components of $T^{(W)}_{ab}$ for our evolution equations are

$$\begin{aligned} T^{(W)}_{ur}(u, r) &= \frac{e^{2\beta}(1 - W^2)^2 + 2rVW_{,r}^2}{2r^4}, \\ T^{(W)}_{rr}(u, r) &= 2\frac{W_{,r}^2}{r^2}. \end{aligned} \tag{2.29}$$

We now use the Einstein's Equations (2.16) and the expression for $T_{ab}^{(W)}$ given by Equation (2.29) and obtain the hypersurface equations

$$\begin{aligned} \beta_{,r} &= 4\pi \frac{W_{,r}^2}{r}, \\ m_{,r} &= \frac{2\pi}{r^2}((W^2-1)^2 + 2r(r-2m)W_{,r}^2). \end{aligned} \tag{2.30}$$

2.3.4.B Wave Equation

Following [4], W obeys the wave equation in the 2-dimensional spacetime reduced by the spherical symmetry, with a potential term, namely

$$\Box_h W = e^{-2\beta}\left[\left(\frac{V}{r}\right)_{,r}\partial_r - 2\partial_u\partial_r + \frac{V}{r}\partial_{rr}\right]W = -\frac{W(1-W^2)}{r^2}. \tag{2.31}$$

Using Equation (2.11), this can be rewritten as

$$W_{,ur} = \frac{e^{2\beta}}{2r^2}\left[W - W^3 + 2W_{,r}(m - rm_{,r} + r(r-2m)\beta_{,r}) + r(r-2m)W_{,rr}\right]. \tag{2.32}$$

We can then use Equation (2.32) to perform our time evolution and find $W_{,r}$ on slices of constant u. Similarly to the scalar field collapse, our evolution system of equations will be composed of two EFE (Equations (2.30)) and the wave equation originated by the collapsing field (Equation (2.32)).

2.3.5 Asymptotic Quantities

In this section, we explore the asymptotic quantities we aim to study within our work, namely the Bondi Mass and the news function.

2.3.5.A Bondi Mass

In GR, there are various definitions of mass that are applicable under different circumstances. This happens because gravitational energy may not be unambiguously localized. However, it is possible to rigorously define mass in asymptotically flat spacetimes, which is the case in this work, as well as in Anti-de Sitter.

As we will see in this section, the Bondi mass is one such global mass definition. It represents all the mass present on a null hypersurface of constant u. Because this hypersurface doesn't intersect any of the radiation emitted prior to the retarded time u, the result is that this mass can only decrease with increasing retarded time u, as we will soon see.

On the other hand, the Arnowitt-Deser-Misner (ADM) mass is another possible global definition which is used when we are dealing with Cauchy slices in an asymptotically flat spacetime. It represents all the mass present on a spacelike hypersurface of constant t. In this case, the hypersurface intersects both the body that is losing mass as a consequence of radiation loss, as well as the radiation emitted. This means that the ADM mass captures both the radiation and the central body mass, resulting in a conserved quantity. [9]

If we define the total energy enclosed by a surface, this energy definition is said to be quasilocal. The Misner-Sharp mass (Equation (2.11)) is one such quasilocal energy definition.

Assuming initial data that is smooth at $\mathscr{I}^+$, one can expand ϕ in powers of $1/r$ at $\mathscr{I}^+$.

$$\phi(u,r) = \frac{c(u)}{r} + \frac{c_{NP}}{r^2} + \mathcal{O}(r^{-3}). \tag{2.33}$$

Inserting the expansion (2.33) into the hypersurface equations (2.17) one gets

$$\begin{aligned} \beta(u,r) &= H(u) - \frac{\pi c^2(u)}{r^2} + \mathcal{O}(r^{-3}), \\ V(u,r) &= e^{2H(u)}\left(r - 2M(u) + \frac{\pi c^2(u)}{r}\right) + \mathcal{O}(r^{-2}), \end{aligned} \tag{2.34}$$

where $H(u)$ and $M(u)$ are integration constants. Note that $H(u) = \lim_{r\to\infty} \beta(u,r)|_{u=const}$. Thus, recalling the definition of the Misner-Sharp mass function (2.11), one can see that $m(u,r)$ has an asymptotic expression of

$$m(u,r) = M(u) - \frac{\pi c(u)^2}{r} + \mathcal{O}(r^{-2}), \tag{2.35}$$

yielding $M(u) = \lim_{r\to\infty} m(u,r)|_{u=const}$, which is defined as the Bondi mass $m_B(u) \equiv M(u)$. In an isolated system, outgoing waves can radiate physical energy to $\mathscr{I}^+$. Therefore, the Bondi mass is in general not conserved in retarded time. In fact, the Bondi mass is monotonic in u. The EFE give us an expression for the mass change that can be written as

$$m_{,u} = -4e^{-2\beta}\pi r^2 T_{00}(u,r) + 8\pi r T_{01}(u,r)(r-2m) - 2\pi e^{2\beta}(r-2m)^2 T_{11}(u,r). \tag{2.36}$$

Note that Equation (2.36) is valid for any general matter model. For the case of a scalar field collapse, T_{ab} is given by Equation (2.15). Introducing the coordinate transformation defined by Equation (2.13), Equation (2.36) can be rewritten as

$$m_{,u} = 4\pi\psi_{,u}\left((-1+x)(x+2\frac{-1+x}{x^2}m)(\psi+(-1+x)x\psi_{,x}) - e^{-2\beta}\psi_{,u}\right), \tag{2.37}$$

which yields the following limit for $x \to 1$ at $\mathscr{I}^+$:

$$m_{,u} = -4\pi e^{-2\beta}\psi_{,u}^2. \tag{2.38}$$

In the case of a Yang-Mills field collapse, T_{ab} is given by Equation (2.29) and the mass loss formula can be written as

$$m_{,u} = -8e^{-2\beta}\pi\xi_{,u}^2 + \frac{2\pi}{r^3}(r-2m)(4e^{2\beta}\xi^2 + 4e^{2\beta}\xi^3 + e^{2\beta}\xi^4 + 4r^2\xi_{,r}\xi_{,u}), \tag{2.39}$$

which at $\mathscr{I}^+$ is simply

$$m_{,u} = -8\pi e^{-2\beta}\xi_{,u}^2. \tag{2.40}$$

We can conclude that the Bondi mass is monotonically decreasing in the case of both fields. This is as expected since no mass can enter our compactified domain.

2.3.5.B News Function

The news function can be defined as

$$N(u_C) = e^{-2H(u_C)}\dot{c}(u_C), \tag{2.41}$$

where u_C denotes central time, i.e., the proper time at the centre of spherical symmetry. Both the Bondi mass and the news function are radiation quantities which we want to study at $\mathscr{I}^+$. We denote the asymptotically flat Bondi time by u_B. In [1], it is shown that the relation between central and Bondi time in the limit $r \to \infty$ is

$$du_B = e^{2H}du_C, \tag{2.42}$$

where $H = \beta(u_C, \infty)$ and $\lim_{r\to\infty}\frac{V}{r}(u_C, r) = e^{2H}$. As discussed in [1], H indicates redshift. We can argue that if $H \to \infty$, then a finite amount of central time u_C corresponds to an infinite amount of time u_B (see Equation (2.42)). This means that light rays being emitted from the centre are infinitely redshifted. Using (2.41) and (2.42) one obtains

$$N(u_B) = \frac{dc}{du_B}, \tag{2.43}$$

Equation (2.43) will then be used to measure the radiation that reaches an observer located at future null infinity $\mathscr{I}^+$, in relation to its time u_B.

2.4 Related Work

In this section, we aim to give an overview of relevant previous works on critical collapse. The foundations of critical phenomena in gravitational collapse were first laid by Choptuik in 1993 [6]. As already discussed, Choptuik found that at the threshold of black hole formation the dynamics of the system become simple and universal in some aspects, despite the complicated form of the EFE.

Later on, studies of global aspects of critical collapse have been carried out by Pürrer, et al. [7]. A self-gravitating massless scalar field in spherical symmetry was evolved numerically, using a compactified grid, just like this work aims to do. Radiation quantities were investigated and they were found to reflect the DSS behaviour.

The algorithm used by Pürrer, et al. is based on the work of Gómez and Winicour [10], who propose the integration of the wave equation over the null parallelogram Σ spanned by four vertices. In this work, we will instead implement an integration scheme based on the Runge-Kutta integration method along null hypersurfaces of constant u. For the time integration we use a Runge-Kutta integrator along with the method of lines. The advantage of our approach is that the methods are more general and can easily be reused in future codes. Moreover, we implement a code that is globally fourth-order accurate.

Our aim is to extend the work by Pürrer, et al. by considering a different collapsing model, namely a Yang-Mills field.

In fact, Gundlach, et al. [8] have studied the critical collapse of two interacting fields in spherical symmetry, a scalar field and a Yang-Mills field. They find that by fine-tuning, the scalar field always dominates on sufficiently small scales. Thus, they conjecture the existence of a “quasi-discretely self-similar” solution shared by the two fields, equal to the Choptuik solution at infinitely small scales and the known Yang-Mills critical solution at large scales, with a gradual transition from one field to the other. This solution is found to act as the critical solution for any mixture of scalar field and Yang-Mills initial data.

In this work we’re dealing with a spacetime foliation based on outgoing null hypersurfaces (see Section 3). We then perform spatial compactification of the coordinate r defined along our constant u hypersurfaces. Our goal is to compare our results of a Yang-Mills collapse with the ones obtained through a foliation based on a hyperboloidal evolution of a Yang-Mills field, as carried out by Rinne and Maliborski [11–13].

In fact, the collapse of a Yang-Mills field has been studied as a CIVP, with an evolution based on compactified null hypersurfaces [14]. However, such work focuses only on the late-time behaviour of subcritical evolutions and here we are interested in critical evolutions.

3

Numerical Methods

Contents

3.1 Characteristic Initial Value Problem 23
3.2 Scalar Field Evolution Scheme 23
3.3 Yang-Mills Field Evolution Scheme 24
3.4 Finite Differencing 25
3.5 Artificial Dissipation 26
3.6 Truncation Error Matching 27
3.7 Analytic Mesh Refinement 28
3.8 CFL-Stability Condition 29
3.9 Code Validation 30

In this section, we discuss the necessary methods used to implement the gravitational collapse we want to study. First, we discuss spacetime foliation and initial data. We then derive the concrete physical setup and the evolution equations using `Mathematica`. After that, we specify the numerical methods used in order to implement our equations. Finally, we discuss convergence tests to validate our numerical results.

3.1 Characteristic Initial Value Problem

The CIVP plays an important role in the field of numerical relativity and our code will be based on such a problem. An initial value problem consists of finding a solution of a partial differential equation when data for the unknown functions in specified on a suitable initial hypersurface [15].

The common Cauchy problem consists of an initial value problem in which the initial data is specified on a space-like hypersurface. This is analogous to solving the Poisson equation: the constraint is given on some spatial boundary and then the equation is integrated to find the value of the functions elsewhere.

In the case of a CIVP, the data is given on one or more null hypersurfaces. In this case, the equations of the problem can be written as ordinary differential equations along characteristic curves, which is often called the method of characteristics. We can think of these equations as propagation equations. Thus the constraints are much simpler in the characteristic case [16].

The bicharacteristics of a massless scalar field are null geodesics [1]. This essentially means that the scalar field propagates at the speed of light and thus, disturbances in our field will propagate along null geodesics. This indicates a foliation of spacetime based on a family of non-intersecting null hypersurfaces. Our CIVP will be solved by specifying on an initial null hypersurface the value of the field we'll be evolving.

In this work, we're then solving our set of equations based on a characteristic foliation. This is in opposition to many other works in numerical relativity which work on a $3+1$ decomposition, i.e. spacetime is foliated by spacelike hypersurfaces labelled by their time coordinate t. This is the essence of the ADM formalism. The advantage of working on a characteristic foliation is not only having an efficient evolution system, but also simplifying the study of the causal structure of our solution.

3.2 Scalar Field Evolution Scheme

Our evolution scheme is composed of the equations (2.18), which can be written as

$$\begin{aligned} m_{,x} &= \frac{2\pi(x+2(x-1)m)(\psi+(x-1)x\partial_x\psi)^2}{x^3} \\ \beta_{,x} &= \frac{2\pi(1-x)(\psi+(x-1)x\partial_x\psi)^2}{x^3}. \end{aligned} \tag{3.1}$$

By Taylor expanding these fields we find that at the origin

$$
\begin{aligned}
m_{,x} &\to 0 \\
\beta_{,x} &\to 0,
\end{aligned} \tag{3.2}
$$

which we impose in our code by substituting the right hand side of (3.1) with 0 at the gridpoint $r = 0$.

Additionally, we use Equation (2.24) to determine the evolution of our field in u. Since this equation is singular around the origin, one must find a way to approximate it for $r = 0$. There are three formally singular terms in Equation (2.22), $\frac{V}{r}$, $(\frac{V}{r})_{,r}$ and $(\frac{V}{r})_{,r}\frac{e^{-2\beta\psi}}{r}$. Expanding these three terms around $r = 0$ one finds that the only non zero term is the one in $\frac{V}{r}$. Equation (2.22) then reduces to

$$
-2e^{-2\beta}\psi_{,ru} + e^{-2\beta}\frac{V}{r}\psi_{,rr} = 0 \Leftrightarrow \psi_{,ru} = \frac{V\psi_{,rr}}{2r}. \tag{3.3}
$$

Our state array is going to be $\{m, \beta, \psi, \psi_{,r}\}$. The evolution scheme is the following:

1. Initial data for $\psi_{,r}$ is given on the whole slice. We choose it in such a way that ψ is described by a Gaussian initial pulse, which is smooth and satisfies our regularity conditions (see Section 5.1.2 for details on the initial data);

2. The field ψ is calculated in the whole grid, integrating out $\psi_{,r}$ and setting $\psi = 0$ at the origin;

3. $m(u, x)$ and $\beta(u, r)$ are computed on the whole slice using Equations (3.1). At each timestep $m(u, x)$ and $\beta(u, r)$ are both set to 0 at the origin;

4. A timestep is taken. Use Equation (2.24) to calculate $\psi_{,r}$ at the next timestep;

5. Steps 2, 3 and 4 are repeated until the evolution reaches the final timestep.

3.3 Yang-Mills Field Evolution Scheme

Our evolution scheme is composed of two hypersurface equations (Equations (2.30)) and the wave equation originated by the collapsing field (Equation (2.32)). In order to implement a regularized set of equations, we need to use the W parametrization given by Equation (2.25). Our evolution equations are then expressed in terms of $x^2\chi$ instead of W. For clarity, we introduce an evolution variable $\xi \equiv x^2\chi$. Our evolution variables are then $\{m, \beta, \xi, \xi_{,r}\}$. Using Equation (2.7) and recalling from Section 2.3.3 that $W - 1 = \xi$, the hypersurface equations can be rewritten as

$$
\begin{aligned}
\beta_{,x} =& -\frac{4\pi}{x}(x-1)^3 W_{,x}^2 = -4\pi\frac{(x-1)^3}{x}\xi_{,x}^2, \\
m_{,x} =& \frac{2\pi}{x^2}((W^2-1)^2 + 2(x-1)^2 x(x+2(x-1)m)W_{,x}^2), \\
=& \frac{2\pi}{x^2}(\xi^2(2+\xi)^2 + 2(x-1)^2 x(x+2(x-1)m)\xi_{,x}^2.
\end{aligned} \tag{3.4}
$$

The wave equation for the W field can be rewritten as a function of our evolution variables in a compactified domain as

$$
\begin{aligned}
\xi_{,ur} =& \frac{e^{2\beta}}{2x^2}(x-1)^2\Bigg(1+\xi-(1+\xi)^3+2(x-1)^2\xi_{,x}(x((x-1)m_{,x}+x\beta_{,x})+m(1+2(x-1)x\beta_{,x})) \\
&+\frac{x}{(x-1)^2}x(x+2(x-1)m)((\chi_{,xx}(x-1)^4)+(2\chi_{,x}(x-1)^3))\Bigg).
\end{aligned} \tag{3.5}
$$

Our evolution scheme is then composed of Equations (3.4) and (3.5). The numerical scheme is the following:

1. Initial data is given for $\xi_{,r}$. We choose it in such a way that ξ describes a Gaussian initial pulse;
2. The field ξ is calculated in the whole grid, integrating out $\xi_{,r}$ and setting $\xi = 0$ at the origin;
3. The metric functions m and β are calculated in the whole grid by solving Equations (3.4), and setting both m and $= \beta$ to 0 at the origin;
4. A timestep is taken. We solve for $\xi_{,r}$ on the next timestep slice using Equation (3.5);
5. Steps 2 to 4 are repeated until the evolution reaches the final timestep.

3.4 Finite Differencing

Finite differencing is one of the most widely used methods for approximating derivatives. The basic idea of finite differencing approximations is to substitute the continuous spacetime with a set of discrete points. This set of points is denominated the computational grid or mesh.

In general a finite difference operator acting upon $\hat{u}$ and gridpoint labeled by i can be written as a weighted sum of grid function values [17]:

$$
\mathcal{D}\hat{u}_i = \ldots + a_{i-2}\hat{u}_{i-2} + a_{i-1}\hat{u}_{i-1} + a_i\hat{u}_i + a_{i+1}\hat{u}_{i+1} + a_{i+2}\hat{u}_{i+2} + \ldots, \tag{3.6}
$$

where a_n are constants. To determine the value of these coefficients, we Taylor expand the $u(x)$ function around $x = x_i$ such that:

$$\begin{aligned}\mathcal{D}\hat{u}_i = \ldots &+ a_{i-2}\left(u + u'(-2h) + \frac{u''}{2!}(-2h)^2 + \frac{u'''}{3!}(-2h)^3 + \ldots\right)\\ &+ a_{i-1}\left(u + u'(-h) + \frac{u''}{2!}(-h)^2 + \frac{u'''}{3!}(-h)^3 + \ldots\right)\\ &+ a_i u\\ &+ a_{i+1}\left(u + u'(h) + \frac{u''}{2!}(h)^2 + \frac{u'''}{3!}(h)^3 + \ldots\right)\\ &+ a_{i+2}\left(u + u'(2h) + \frac{u''}{2!}(2h)^2 + \frac{u'''}{3!}(2h)^3 + \ldots\right) + \ldots,\end{aligned} \tag{3.7}$$

in which $u \equiv u(x_i)$ and $u' \equiv \frac{du(x)}{dx}|_{x=x_i}$, etc. We can reorder the terms in (3.7) to

$$\begin{aligned}\mathcal{D}\hat{u}_i = &\, u\left(\ldots + a_{i-2} + a_{i-1} + a_i + a_{i+1} + a_{i+2} + \ldots\right)\\ &+ u'h\left(\ldots - 2a_{i-2} - a_{i-1} + a_{i+1} + 2a_{i+2} + \ldots\right)\\ &+ u''\frac{h^2}{2!}\left(\ldots + 2^2a_{i-2} + a_{i-1} + a_{i+1} + 2^2a_{i+2} + \ldots\right)\\ &+ u'''\frac{h^3}{3!}\left(\ldots - 2^3a_{i-2} - a_{i-1} + a_{i+1} + 2^3a_{i+2} + \ldots\right)\\ &+ \ldots.\end{aligned} \tag{3.8}$$

We define the coefficients multiplying the m^{th} derivative of u by S_m, so we can write (3.8) as

$$\mathcal{D}\hat{u}_i = uS_0 + u'hS_1 + u''\frac{h^2}{2!}S_2 + u'''\frac{h^3}{3!}S_3 + \ldots. \tag{3.9}$$

The second and fourth-order accurate finite difference schemes used to approximate derivatives on our grid are respectively given by

$$\begin{aligned}u' = &\frac{u_{i-1} - u_{i+1}}{2h} - \frac{h^2}{6}u^{(3)}\\ u' = &\frac{u_{i-2} - 8u_{i-1} + 8u_{i+1} - u_{i+2}}{12h} + \frac{h^4}{30}u^{(5)}.\end{aligned} \tag{3.10}$$

3.5 Artificial Dissipation

In GR, many of the systems of equations we work with are non-linear. For this reason, many numerical methods used become slightly unstable because of coefficients that depend on dynamical variables and lower-order terms [18]. Consequently, one ought to introduce dissipative terms to the numerical scheme — i.e. add artificial dissipation. Kreiss-Oliger dissipation is used to damp out the formation of high frequency modes [19].

In case of an original scheme of second-order we need to add fourth-order dissipation, whereas in an original scheme of fourth-order we need to add sixth-order dissipation. Following the work of

Alcubierre [18], we assume we have a finite difference scheme given by

$$u_m^{n+1} = u_m^n + \Delta t S\left(u_m^n\right), \tag{3.11}$$

with $S(u_n)$ some spatial finite difference operator and m the accuracy of the original scheme. We modify this scheme by adding a term of the form

$$u_m^{n+1} = u_m^n + \Delta t S\left(u_m^n\right) - \epsilon \frac{\Delta t}{\Delta x}(-1)^N \Delta_x^{2N}\left(u_m^n\right), \tag{3.12}$$

where $\Delta_x^{2N} := \left(\Delta_x^+ \Delta_x^-\right)^N$ is the $2N$ centered difference operator and $\epsilon > 0$.

In a second-order accurate code we have $2N = 4$, whereas in a fourth-order accurate code $2N = 6$. For each of these two cases respectively, the centered difference operator are then given by

$$\begin{aligned}\Delta_x^4 u_m^n =& u_{m+2}^n - 4u_{m+1}^n + 6u_m^n - 4u_{m-1}^n + u_{m-2}^n \\ \Delta_x^6 u_m^n =& u_{m+3}^n - 6u_{m+2}^n + 15u_{m+1}^n - 20u_m^n + 15u_{m-1}^n - 6u_{m-2}^n + u_{m-3}^n.\end{aligned} \tag{3.13}$$

We then add a new term to the original differential equation that vanishes in the continuum limit and thus doesn't spoil the accuracy of the scheme, when using an appropriate ϵ.

3.6 Truncation Error Matching

Our general finite difference scheme used to approximate derivatives on our grid is given by Equation (3.10), which we rewrite here

$$\begin{aligned}u' =& \frac{u_{i-1} - u_{i+1}}{2h} - \frac{h^2}{6}u^{(3)} \\ u' =& \frac{u_{i-2} - 8u_{i-1} + 8u_{i+1} - u_{i+2}}{12h} + \frac{h^4}{30}u^{(5)}.\end{aligned}$$

At the first and second gridpoints of our grid, our fourth-order accurate finite difference operator is not defined, thus we need to use a different stencil, lopsided by two and one gridpoints respectively, and we need to make sure that the error terms match.

Let us now focus on the case of a code that is globally fourth-order accurate. In Equation (3.9), we see that we need to have $S_0 = 0 = S_2 = S_3 = S_4$, $S_1 = \frac{1}{h}$ and $S_5 = \frac{-5!}{30h}$. Solving for these six equations one finds the a_i coefficients, yielding in the following finite differences for the second and first gridpoint respectively:

$$
\begin{aligned}
u' &= \frac{-2u_{i-1} - 15u_i + 28u_{i+1} - 16u_{i+2} + 6u_{i+3} - u_{i+4}}{12h} + \frac{h^4}{30}u^{(5)}, \\
u' &= \frac{-27u_i + 58u_{i+1} - 56u_{i+2} + 36u_{i+3} - 13u_{i+4} + 2u_{i+5}}{12h} + \frac{h^4}{30}u^{(5)}.
\end{aligned}
\tag{3.14}
$$

As discussed in Section 3.5, in a fourth-order accurate code, the dissipation operator is sixth-order accurate and the coefficients used correspond to the ones of the finite difference scheme to approximate a sixth derivative with second-order accuracy (see Equation (3.12)), which has an error term:

$$
u^{(6)} = \frac{u_{i-3} - 6u_{i-2} + 15u_{i-1} - 20u_i + 15u_{i+1} - 6u_{i+2} + u_{i+3}}{h^6} + \frac{h^2}{4}u^{(8)}. \tag{3.15}
$$

Similarly to what we did with our approximated derivative operator, we also need to make sure that the dissipation calculated in the first, second and third gridpoints match with the dissipation in the rest of the grid. In this case, we need $S_6 = \frac{6!}{h^6}$ and $S_8 = \frac{-8!}{4h^6}$. Solving for these nine equations we find:

$$
\begin{aligned}
\Delta_x^6 u_m^n &= \frac{19u_i - 142u_{i-1} + 464u_{i-2} - 866u_{i-1} + 1010u_i - 754u_{i+1} + 352u_{i+2} - 94u_{i+3} + 11u_{i+4}}{2h^6} \\
\Delta_x^6 u_m^n &= \frac{11u_{i-1} - 80u_{i-2} + 254u_{i-1} - 460u_i + 520u_{i+1} - 376u_{i+2} + 170u_{i+3} - 44u_{i+4} + 5u_{i+5}}{2h^6} \\
\Delta_x^6 u_m^n &= \frac{5u_{i-2} - 34u_{i-1} + 100u_i - 166u_{i+1} + 170u_{i+2} - 110u_{i+3} + 44u_{i+4} - 10u_{i+5} + u_{i+6}}{2h^6},
\end{aligned}
\tag{3.16}
$$

with $u^{(6)} = \Delta_x^6 u_m^n + \frac{h^2}{4}u^{(8)}$. We now use the same reasoning for the simpler case of a second-order accurate code. In this case, the finite differences operator for the first gridpoint is given by

$$
u' = \frac{-4u_i + 7u_{i+1} - 4u_{i+2} + u_{i+3}}{2h} - \frac{h^2}{6}u^{(3)}, \tag{3.17}
$$

which matches the error term in (3.10). The dissipation operator (3.13) in the first and second gridpoints is given by

$$
\begin{aligned}
\Delta_x^4 u_m^n =& \frac{19u_i - 89u_{i+1} + 166u_{i+2} - 154u_{i+3} + 71u_{i+4} - 13u_{i+5}}{6h^4}, \\
\Delta_x^4 u_m^n =& \frac{13u_{i-1} - 80u_{i-2} + 254u_{i-1} - 460u_i + 520u_{i+1} - 376u_{i+2} + 170u_{i+3} - 44u_{i+4} + 5u_{i+5}}{6h^4}.
\end{aligned}
\tag{3.18}
$$

3.7 Analytic Mesh Refinement

Since studying critical phenomena requires high numerical precision, we perform a coordinate transformation from x to $\tilde{x}$ [20] through

$$
x(\tilde{x}) = \Theta \arctan((\tilde{x} - k)n) + m, \tag{3.19}
$$

where A, n, k and m are constants that we choose in order to control the resolution we want towards the boundaries in each situation. In general, we fix $\Theta = 0.35$, $n = 5$, $k = 0.7$ and $m = 0.5$, unless otherwise stated.

In our simulations, our grid is then evenly spaced in $\tilde{x}$, where we perform our finite differences. This corresponds to a grid that is unevenly spaced in x in such a way that we have more resolution in the regions of interest, both at the origin and future null infinity. Note that with this choice of coordinates the resolution at the boundaries is higher, and approximately constant, so we choose the grid parameters according to the resolution we are looking to have in these regions.

Using a grid with more resolution towards the boundaries has often been reported as a way to reduce interpolation errors. When we are dealing with interpolation of a data set with equispaced interpolation points, the polynomial interpolation becomes less reliable towards the boundaries of our domain, where it shows oscillations between consecutive interpolation points. This is known as Runge's Phenomenon. It's crucial to control Runge's phenomenon especially in codes that use integration methods of fourth-order and higher, since in these cases we need to evaluate our interpolation function in points that don't belong to the set of interpolating points.

A common solution to mitigate Runge's Phenomenon is to use a grid that is composed of Chebyshev Nodes which are given by

$$x(\tilde{x}) = \frac{1}{2}\left(1 + \cos\left(\pi(1 - \tilde{x})\right)\right) \tag{3.20}$$

in an interval $[0, 1]$. In our case, we still want to compute our physical quantities in our coordinate x and using Equation (3.20) would lead to a null Jacobian at the boundaries, resulting in a singular set of hypersurface equations.

Ultimately, using Equation (3.19) will be more appropriate in our case, as we still have more resolution towards the boundaries like in the Chebyshev nodes, and expect to mitigate Runge's Phenomenon, plus the Jacobian of this transformation is finite everywhere in our domain.

We will further analyse how these grid choices impact numerical accuracy in the results Section 5.1.1, particularly by investigating numerical convergence in different grid schemes.

3.8 CFL-Stability Condition

The stability condition by Courant-Friedrichs-Levy (CFL) is a necessary condition for stability while solving certain partial differential equations numerically.

Essentially, the CFL condition expresses that the full numerical domain of dependence must contain the physical domain of dependence. Therefore, the distance that any information travels during the timestep length within the mesh (Δt) must be lower than the distance between mesh elements (Δx).

The CFL-condition has the following form:

$$C = \frac{v\Delta t}{\Delta x} \leq C_{max}, \tag{3.21}$$

in which the dimensionless number C is called the Courant number and $v = \frac{dx}{du}$ is the magnitude of the velocity. We can derive the value of $\frac{dx}{du}$ in our problem by taking $d\theta = d\phi = 0$ in the line element (Equation (2.6)). This yields $\frac{dr}{du} = \frac{-V}{2r}$, which can be rewritten in terms of m and x as

$$\frac{dx}{du} = \frac{(1-x)^3 e^{2\beta}(2m/x - \frac{1}{1-x})}{2}. \tag{3.22}$$

We start the evolution with $\Delta u = 0.5\Delta x$ on the first iteration. At each iteration, Δu is then updated according to $\Delta u = 0.5\Delta x(\frac{dx}{du})^{-1}$. This ensures that the physical domain of dependence is contained within the numerical domain of dependence.

3.9 Code Validation

Any solution we find numerically is merely an approximation to the *true* solution to a differential equation. We must then study the error in these approximations, to make sure we can trust our numerical solutions. For this purpose, it is usual to perform convergence tests on the code implemented. In this section we describe how we perform such convergence tests.

3.9.1 Norm Convergence Test

The key idea is to compute a solution at two different resolutions Δ_1 and Δ_2 and calculate the solution error [18] as

$$\begin{aligned} \epsilon_{\Delta_1} &= u - u_{\Delta_1}, \\ \epsilon_{\Delta_2} &= u - u_{\Delta_2}. \end{aligned} \tag{3.23}$$

We then compute the norm of each solution error ϵ_1 as

$$Q(t) = \frac{||\epsilon_{\Delta_1}||}{||\epsilon_{\Delta_2}||}, \tag{3.24}$$

where $Q(t)$ is known as the convergence factor. In practise, we do not know the exact solution u, so the best we can do is to prove that our numerical solution converges to some continuum function [18]. For this, we compute our solution in three different resolutions Δ_1, Δ_2 and Δ_3. We then compute relative errors between different resolutions and the convergence factor as

$$Q(t) = \frac{||u_{\Delta_1} - u_{\Delta_2}||}{||u_{\Delta_2} - u_{\Delta_3}||}. \tag{3.25}$$

The core idea here is that in the continuum limit the convergence factor should behave as

$$\lim_{\Delta \to 0} = \frac{\Delta_1^n - \Delta_2^n}{\Delta_2^n - \Delta_3^n} = r^n, \tag{3.26}$$

in which n denotes the numerical accuracy of the methods implemented and $r = \frac{\Delta_1}{\Delta_2}$. Typically, the convergence tests are done with $\Delta_2 = \Delta_1/2$, i.e. $r = 2$.

In the calculation of the convergence factor, we need to choose an appropriate norm in each scenario, as we'll describe when presenting the results of such tests. Naturally, the convergence factor varies throughout the evolution, and thus a curve of $Q(t)$ is studied.

3.9.2 Pointwise Convergence Test

Another possibility is to perform local convergence tests, namely a pointwise convergence test. This is especially useful as it can allow for identification of problems in specific regions (the boundaries, for instance) that can be harming global convergence.

We perform this test by simply plotting the relative errors $u_{\Delta_1} - u_{\Delta_2}$ and $u_{\Delta_2} - u_{\Delta_3}$. In our case, $\Delta_1 = 2\Delta_2$. Looking at Equation (3.26), we plot two curves, $u_{\Delta_1} - u_{\Delta_2}$ and $2^n \times (u_{\Delta_2} - u_{\Delta_3})$, which we expect to overlap over the whole domain. Recall from Section 3.9.1 that n denotes the accuracy of the implemented scheme.

4

Preparatory Work

Contents

4.1 Toy Model 35
4.2 Convergence Tests 36

In this section we go through the implementation of a toy model. This toy model is a simpler version of the system of equations we ultimately want to study. This allows us to implement our methods and test them through convergence tests, before moving on to the gravitational collapse implementation, in Section 5.

4.1 Toy Model

As discussed above, the system we will want to evolve is described by a characteristic code in compactified Bondi coordinates. We first started by implementing a toy model of a simpler model in $1+1$ dimensions, which we'll describe in this section. The goal of this early implementation was to build the evolution code that can later be adapted to the characteristic critical collapse we want to study. As a simpler model is easier to manage than the problem in full GR, we can then analyse its results and ensure that the numerical methods are built in a correct manner and work as expected.

We then want to solve for the evolution of f and g in

$$\begin{aligned}(\partial_t+\partial_x)f &= A(x,t),\\ (\partial_t-\partial_x)g &= 0.\end{aligned} \tag{4.1}$$

$A(x,t)$ denotes a given function which was fixed to $A(x,t)=\sin(t)=\sin(u+x)$. We make this choice so that our system describes a right moving wave. We will work in coordinates $\{u=t-x,x\}$, similar to a compactified version of the Bondi coordinates $\{u,r,\theta,\phi\}$ in spherical symmetry. The evolution is performed by a foliation of spacetime in null slices of constant u, where we solve for our functions f and g. Using `Mathematica`, the evolution equations are found to be of the form

$$\partial_x f=\sin(x+u), \tag{4.2}$$

$$\partial_u g=\frac{1}{2}(\partial_x g(u,x)). \tag{4.3}$$

Note that f describes a right moving wave and g describes a left moving wave. For this reason, we need to specify the value of f at the left boundary (setting it to 0) and g at the right boundary (setting it to $\sin(2\pi/10(2x+u))$), as illustrated in Figure 4.1. Initial data for g is also given in the first timestep of the evolution according to the same expression.

Our numerical grid has length 40 and is discretized in x with resolution $x_{i+1}-x_i=dx=0.2$. The *time* increment du is set to 0.08. Our computational scheme is then the following:

1. Initial data for f is given at the left boundary as $f(x=0)=0$. The value of f for an initial hypersurface of constant $u=0$ is then computed by integrating out on x using Equation 4.2;

2. Initial data for g is given on the whole grid as $g(x,u=0)=\sin(4.0\pi x/10.0)$.

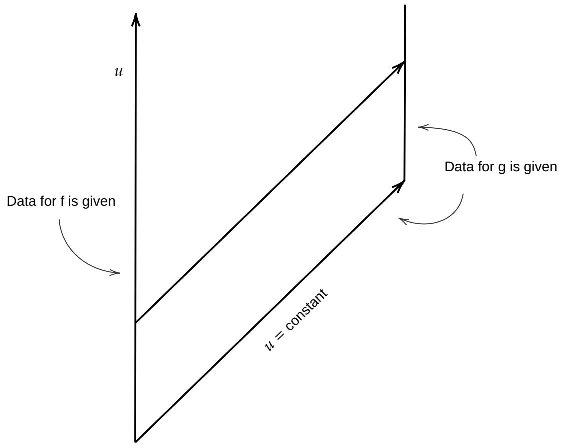

Figure 4.1: Given data for f and g evolution.

3. A timestep $u_{i+1} = u_i + du$ is taken;
4. The value of f and g are calculated at every gridpoint using Equations 4.2 and 4.3 respectively:
   (a) Data for f is given at the left boundary as $f(x=0) = 0$ and integrated out.
   (b) Data for g is given at the right boundary as $\partial_u g = \frac{1}{2}\frac{4\pi}{10}\cos(2\pi/10(2x+u))$ such that $g = \sin(2\pi/10(2x+u))$ at $x = 40$.
5. Steps 3 and 4 are repeated until the evolution reaches the last timestep.

The integrations were performed using a Runge-Kutta integrator of fourth-order and the derivatives were approximated using a fourth-order finite difference scheme. Images of the evolution as well as the code developed (`Julia`, `Python` and `Mathematica` files) can be found at the GitHub repository.

We note that the implementation of this toy model is similar to the code we implement to study the collapse of a scalar field. First of all, since we are dealing with a spherically symmetric collapse, we work only with $(u = t - x, x)$ coordinates like in this toy model. Additionally, at each timestep we have a hypersurface of constant u in which we solve for the values of f and g. In the case of the gravitational collapse, we similarly solve for β, V and ψ. Lastly, the fourth-order accurate methods we built here are the same in our collapse scheme.

4.2 Convergence Tests

The first convergence test implemented here is a pointwise convergence test, as described in Section 3.9. Using the same initial data and evolution equations, the solutions for f and g were computed at three different resolutions: the standard one, with $\Delta_1 = 0.2$, a second one with resolution $\Delta_2 = \Delta_1/2$ and

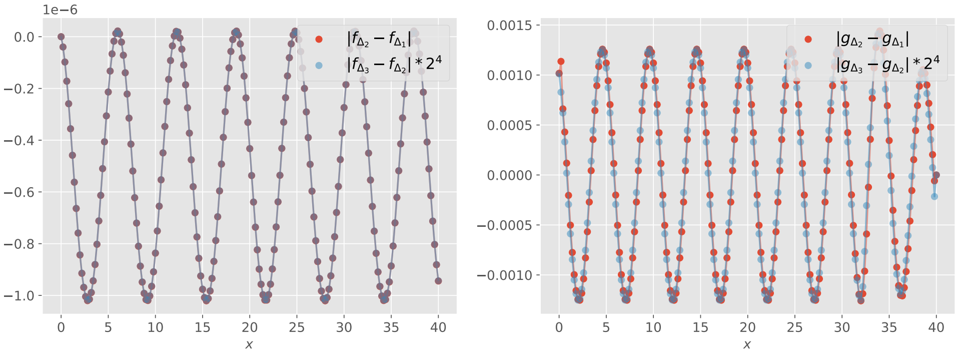

Figure 4.2: Pointwise convergence plots for f and g at last timestep of evolution.

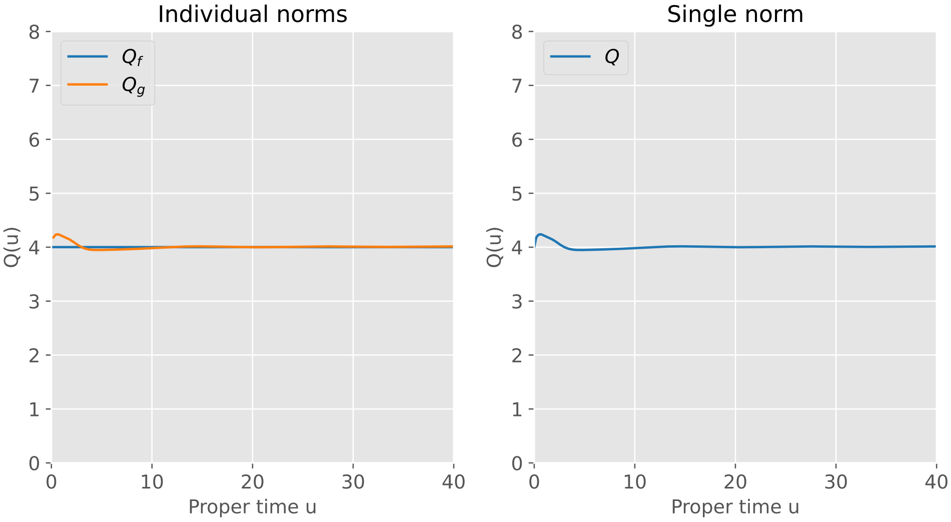

Figure 4.3: Convergence factor Q(t) throughout the evolution. On the left, we show each evolution variable individually, and on the right we show the norm of all variables together.

a third one with $\Delta_3 = \Delta_1/4$. The values of both f and g were compared at the common gridpoints. Both convergence tests are performed after introducing the dissipation operator discussed in Section 3.5.

The left side of Figure 4.2 shows the difference between the solution for f with medium and low resolution, $|f_{\Delta_2} - f_{\Delta_1}|$, as well as the same difference but for high and medium resolution $|f_{\Delta_3} - f_{\Delta_2}|$. The right side of this same Figure shows the same values but for g. The values shown correspond to the last timestep of the evolution.

The L^2 convergence was also investigated by computing the L^2 norm of the errors plotted in Figure 4.2, resulting in a convergence factor Q of

$$Q_f = log_2\left(\left(\frac{\sum(f_{med} - f_{low})^2}{\sum(f_{high} - f_{med})^2}\right)^{\frac{1}{2}}\right) = 4.001, \qquad Q_g = log_2\left(\left(\frac{\sum(g_{med} - g_{low})^2}{\sum(g_{high} - g_{med})^2}\right)^{\frac{1}{2}}\right) = 4.014, \tag{4.4}$$

in the last timestep of the evolution. In Figure 4.3, we show the convergence factor Q calculated at each time step of the basis resolution Δ_1.

Note that, as expected, both convergence tests indicate that both f and g have fourth-order convergence. This is as expected since both functions are computed at each timestep using fourth-order accurate methods. Additionally, the derivative $\partial_x g$ is calculated using a finite difference method of fourth-order and thus g has fourth-order convergence (Equation 4.3).

It was then possible to successfully construct our integration scheme and evolution code, as well as test the convergence of our methods. This is an important starting point for the codes implemented in Section 5.

5

Numerical Results

Contents

5.1 Scalar Field Collapse 41
5.2 Yang-Mills Field Collapse 55

In this section, we present the numerical results of the implementation of the collapse of a scalar field, and then of two toy models of the Yang-Mills field. For the first physical scenario, we start by presenting the results of the convergence tests performed in all code implementations. Then we provide an analysis of critical behaviour, studying the similarity solutions and black hole mass scaling for instance. We investigate global properties of the collapse, analysing the evolution of the Bondi mass and news function. For the Yang-Mills collapse, we present two toy models and test convergence. The field collapse in full GR is also implemented and an analysis of critical solutions is provided. All the code developed (`Julia`, `Python` and `Mathematica` files) can be found at the GitHub repository.

5.1 Scalar Field Collapse

We started by implementing the scalar field collapse in a code that uses methods (namely the Runge-Kutta integrators and finite differencing schemes) that are second-order accurate. We then implement the same code but using fourth-order accurate methods. We finally implement a grid transformation, as discussed in Section 3.7, first using a globally second-order accurate scheme, and lastly a fourth-order accurate one.

5.1.1 Convergence Tests

As discussed in Section 3.9, we now perform two tests: pointwise and norm convergence tests. Because we are in spherical symmetry, we use a norm that takes into consideration the fact that our variables are radial functions. Recall that the evolution variable ψ is itself obtained by rescaling the ϕ scalar field through Equation (2.13). Thus, only the evolution variables m and β need rescaling in the convergence tests. When using Equation (3.25), we simply multiply m and β by r before taking the norm in spherical symmetry.

The convergence test performed gives the result in Figure 5.1. We stop the convergence test when the magnitude of all fields is smaller than 10^{-7}. In this regime, the norm of the errors approaches the double float precision of 15 digits and the computed convergence factor is no longer reliable.

Figure 5.1 shows the convergence factor calculated throughout the evolution. The individual norms stands for the norms of each evolve variable separately, whereas the single norm is obtained by taking the norm of the four variables together, at each timestep. The dotted lines correspond to a grid with 100 points and the solid lines correspond to a grid with 200 points. We can see that as we increase resolution the convergence factor Q gets closer to 2, both for each field individually as for the single norm. These results not only reassure us that our code is globally second-order accurate, but also that this result is better as we increase resolution. As we perform runs that are closer to criticality, we will make runs with 10^4 to 2×10^4 points, which will guarantee the desired numerical convergence.

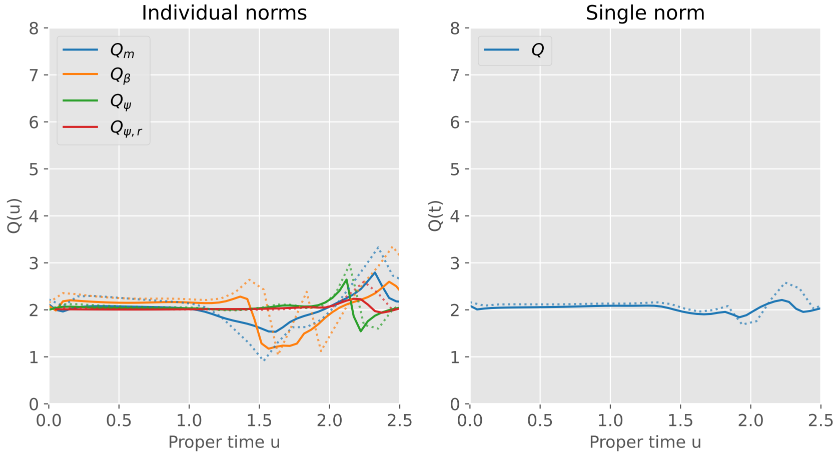

Figure 5.1: Convergence factor Q(t) throughout the evolution for a uniform grid, using a code that is globally second-order accurate. The dotted lines correspond to the result obtained with a grid with 100 points and the solid lines correspond to a grid with 200 points. On the left, we show Q(t) for each evolution variable individually, and on the right we show the norm of all the variables together. An initial pulse of amplitude $A = 0.1$ was considered.

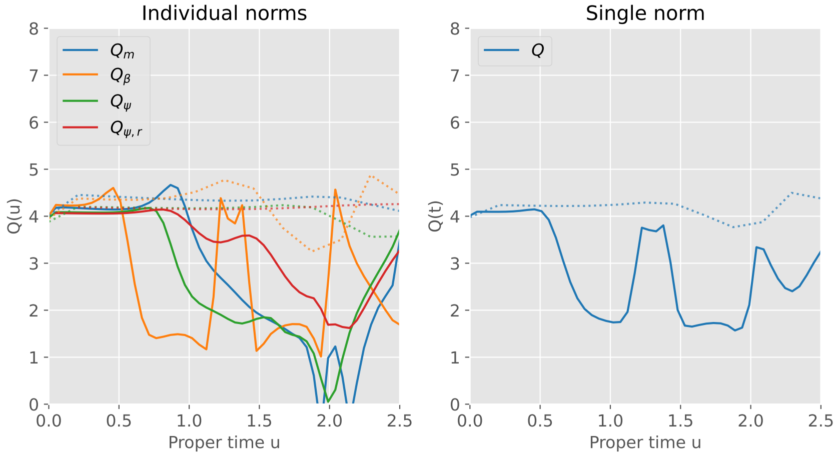

Figure 5.2: Convergence factor Q(t) throughout the evolution for a uniform grid, using a code that is globally fourth-order accurate. The dotted lines correspond to a grid with 100 points and the solid lines correspond to a grid with 200 points. On the left, we show Q(t) for each evolution variable individually, and on the right we show the norm of all the variables together. An initial pulse of amplitude $A = 0.1$ is considered.

Figure 5.2 shows the same convergence test as in Figure 5.1, but calculated with a code that is globally fourth-order accurate. As one can see, clean fourth-order convergence is harder to obtain. Furthermore, it is not clear that increasing resolution leads to better convergence.

In Figures 5.3 and 5.4, we investigate pointwise convergence for the second and fourth-order accurate code respectively. Note that the second-order code shows better pointwise convergence, and that the errors in the fourth-order accurate scheme come from the left boundary. At each timestep β is calculated by integrating out a hypersurface equation that depends on evaluating an interpolation

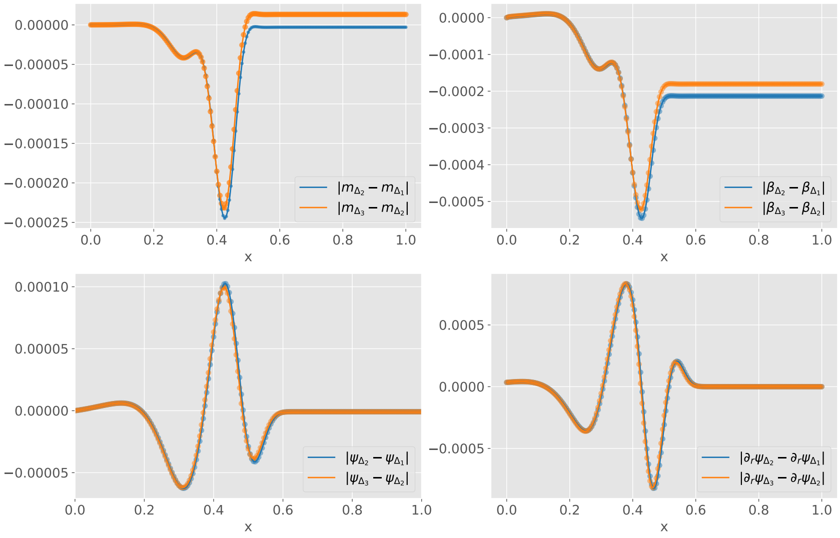

Figure 5.3: Pointwise convergence for each evolution variable. The values presented are computed using a uniform grid, in code that is globally second-order accurate. The timestep presented corresponds to $t = 0.5$. The orange curves are rescaled by a factor of 2^4 (see Section 3.9).

function. This is an indication that Runge's phenomenon is spoiling our convergence. As discussed in Section 3.7, this is common in higher-order schemes, as we must evaluate our interpolating function in midsteps when performing our numerical integration (using a fourth-order accurate Runge-Kutta integrator). This can be mitigated by introducing a grid with more resolution towards the boundaries.

Furthermore, in null foliations of spacetime, it is not straightforward to use parity arguments to improve convergence at the origin. It is not trivial how ghost points should be populated in a compactified domain, hence we resort to a lopsided grid, yielding the interpolation errors at the origin which we already discussed. Some solutions to this problem were implemented. First, one could use a Taylor approximation around the origin in the $\psi = \phi r$ field. Additionally, one could evolve a secondary grid in parallel with twice the resolution, avoiding the need to evaluate the spline in points where we don't know the value of the field, but this is very computationally inefficient. Neither of these approaches were sufficient to mitigate the behaviour shown in Figure 5.4. The best solution was to implement a grid transformation, as described in Section 3.7. By performing this change of coordinates, we now work with a grid with more resolution towards the boundaries, reducing the impact of interpolation errors in this region.

However, do note that the norm of the errors $|\Delta_2 - \Delta_1|$ are much smaller in the fourth-order accurate code ($\approx 2 \times 10^{-5}$, comparing to $\approx 3 \times 10^{-3}$ in the second-order accurate) and this code is able to give much better results than second-order accurate methods, as we'll see in the rest of this section.

We then implement a grid that is non-uniform to study if such setup improves convergence results. This technique is sometimes referred to as analytic mesh refinement, as we define new coordinates that

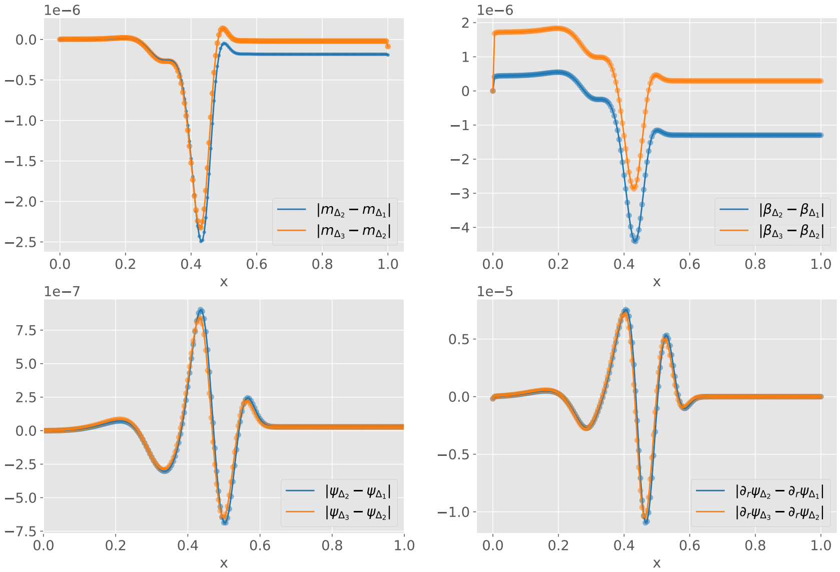

Figure 5.4: Pointwise convergence for each evolution variable. The values presented are computed using a uniform grid, in code that is globally fourth-order accurate. The timestep presented corresponds to $t = 0.5$. The orange curves are rescaled by a factor of 2^4 (see Section 3.9).

are fixed over time and that cluster in regions of interest. As described in Section 3.7, we implement a grid with points $\tilde{x}$ given by Equation (3.19).

Figures 5.5 and 5.6 show the norm convergence test obtained using such grid, using second and fourth-order accurate methods respectively. Comparing with Figures 5.1 and 5.2, we see that the second-order accurate code performs as well in the uniform grid as in the non-uniform one. The differences are more striking in the fourth-order accurate code: the non-uniform grid produces a much cleaner convergence. Additionally, note that increasing resolution does indeed result in a clear convergence factor.

This confirms the above discussion about convergence in higher-order schemes, in which interpolating functions have to be evaluated in points outside of the interpolating set of points. Runge's phenomenon leads to worse convergence in uniform grids, but using analytic mesh refinement we are able to obtain much better results and diminish this phenomenon.

5.1.2 Initial Data and Diagnostics

We consider the collapse of initial data that is Gaussian-like, given by Equation (5.1). We fix $r_0 = 0.7$ and $\sigma = 0.3$ and study the influence of changing the amplitude A, our criticality parameter. We are then studying the collapse of one-parameter families of initial data for different numbers of gridpoints N.

$$\phi(u_0, x) = Ar(x) \exp\left[-\left(\frac{r(x) - r_0}{\sigma}\right)^2\right], \tag{5.1}$$

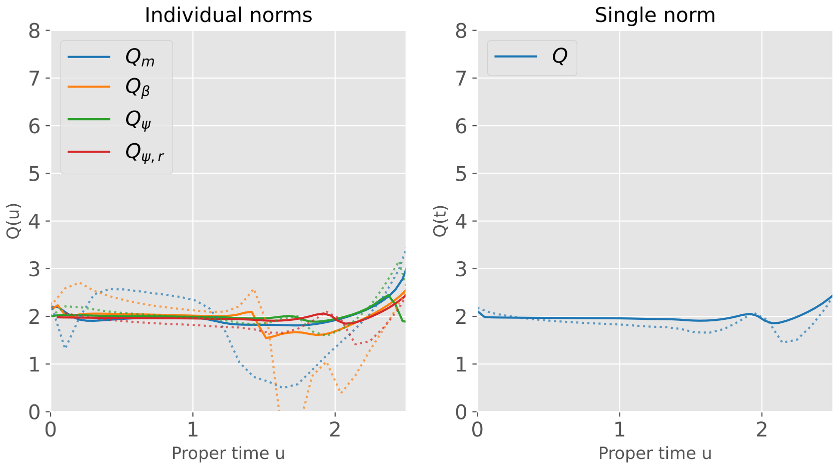

Figure 5.5: Convergence factor Q(t) throughout the evolution for an unevenly spaced grid in x. The dotted lines correspond to a grid with 200 points and the solid lines correspond to a grid with 400 points. On the left, we show Q(t) for each evolution variable individually, and on the right we show the norm of all the variables together. An initial pulse of amplitude $A = 0.01$ is considered.

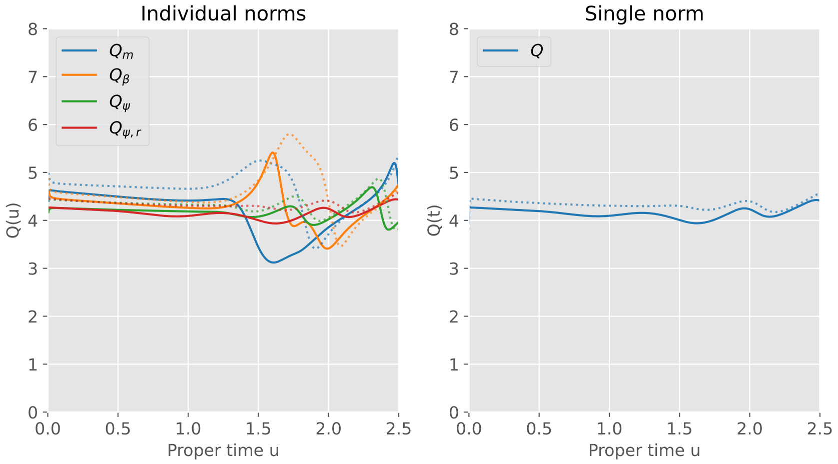

Figure 5.6: Convergence factor Q(t) throughout the evolution for an unevenly spaced grid in x. The dotted lines correspond to a grid with 100 points and the solid lines correspond to a grid with 200 points. On the left, we show Q(t) for each evolution variable individually, and on the right we show the norm of all the variables together. An initial pulse of amplitude $A = 0.01$ is considered.

where $r(x) = \frac{x}{1-x}$. We first implement the collapse of initial data in an uncompactified setup. Because we want to include both the origin and future null infinity in our numerical grid, we then implement the compactification through $r(x) = \frac{x}{1-x}$. We compare both evolutions to confirm correct implementation.

In practice, we detect the formation of an apparent horizon by monitoring the value of the compactness $\frac{2m}{r}$ throughout the evolution, with $\frac{2m}{r} = 1$ signifying the presence of an apparent horizon. Since we use a characteristic formulation, our slices do not penetrate apparent horizons. As it is common practice, we *soften* the condition by using $\frac{2m}{r} > 0.7$ as the numerical condition to mark evolutions as supercritical.

Evolutions in which we have the formation of an apparent horizon are called supercritical, whereas evolutions that disperse are subcritical. We are interested in the evolutions lying between these two scenarios, the critical solutions. We find the critical amplitude that produces such evolutions by performing a bisection search in the parameter A.

Evolutions closer to criticality are slowed down by a CFL-type condition, when the compactness starts increasing, as discussed in Section 3.8.

As we tune closer to the critical parameter A^*, our solution will approach the critical solution found by Choptuik and exhibit characteristics of critical phenomena, as discussed in Section 2.1. One of these characteristics is discrete self-similarity of the collapsing field solution. This self-similarity is characterised by an echoing period Δ, which we'll extract from our evolutions.

Based on our Bondi coordinates $\{u, r, \theta, \phi\}$, we define the specific DSS-adapted time coordinate as

$$T = -\ln(u^* - u), \tag{5.2}$$

where u is some measure of time which is usually taken as the proper time at the origin, and u^* is the the accumulation time, at which the curvature diverges [21]. T is then what we will call the similarity time. Note that T is defined for a constant $u^* > 0$ and $u < u^*$ [4].

The accumulation time u^* can be estimated by taking two pairs of consecutive zero-crossings of the magnitude of the scalar field ϕ at the origin, (u_n,u_{n+1}) and (u_m,u_{m+1}). Assuming that each pair differs in half of the period $\Delta/4$, we can solve for the accumulation time obtaining

$$u^* = \frac{u_n u_{m+1} - u_{n+1} u_m}{u_n - u_{n+1} - u_m + u_{m+1}}. \tag{5.3}$$

The same reasoning can be applied to provide an estimate for the echoing period Δ [21] given by:

$$\Delta = 2\ln\left(\frac{u^* - u_n}{u^* - u_{n+1}}\right). \tag{5.4}$$

5.1.3 Identification of Critical Behaviour

We start by performing the bisection search in a code that is globally second-order accurate and then on a code that is globally fourth-order accurate. We aim to first find the critical amplitude A^*, in order to then extract relevant quantities of critical solutions, such as the self-similarity echoing period Δ and the accumulation time u^*. For a near-critical solution, the approximate value of the accumulation time defines an approximate location (i.e. advanced time) of the Self-Similarity Horizon (SSH).

The results of such bisections are presented in Table 5.1 for uniform grids. Because critical phenomena requires using high numerical accuracy, we perform some runs using a non-uniform grid, as described in Section 3.7. The results of such runs using analytic mesh refinement are presented in Table 5.2.

Table 5.1: Critical parameters obtained for the same family of initial data, with different grid setups and code accuracy. All values presented are calculated for evenly spaced grids with different basis resolutions N. A^* denotes the critical amplitude, u^* denotes the accumulation time and Δ is the self similarity echoing period defined in Section 2.1.2. All evolutions are fine-tuned up to 18 decimal places, besides the one with N=2×10^5 which is fine-tuned to 10 decimal places.

N	A^*	u^*	Δ	Code convergence
2000	0.12464719767642393	2.043029733759220	3.47967738	$\mathcal{O}$(2)
2000	0.12465049029170885	2.043759831375838	3.44743487	$\mathcal{O}$(4)
10000	0.12465050144332973	2.043588707426901	3.46520655	$\mathcal{O}$(4)
20000	0.12465050165997141	2.043591312852050	3.46506464	$\mathcal{O}$(4)

Table 5.2: Critical parameters obtained for the same family of initial data, with different grid setups and code accuracy. All values presented are calculated for non-uniform grids with different basis resolutions N. The grid parameters in Equation (3.19) are set to $\Theta = 0.44$, $n = 4.0$, $k = 0.47$, $m = 0.5$ in all runs. A^* denotes the critical amplitude, fine tuned up to 10 decimal places, u^* denotes the accumulation time and Δ is the self-similarity echoing period defined in Section 2.1.2.

N	A^*	u^*	Δ	Code convergence
1000	0.12491048189863257	2.0797540091275646	3.2148131200000005	$\mathcal{O}$(2)

Regarding the results shown in Table 5.1, we first notice that the more resolution we use, the higher the critical amplitude. As one would expected, using more resolution makes it easier to resolve critical phenomena. Similarly, using methods that have higher accuracy also results in slightly higher critical amplitudes. This is because as we increase resolution we are able to better resolve the regions of high curvature. Moreover, the values obtained for the accumulation time u^* are very close to each-other, no matter the setup considered.

Regarding the echoing period Δ, we obtain $\Delta \approx 3.4$. This result is approximately the same as the literature result [7] for the collapse of a massless scalar field. Note that our results are better when we use a code that is fourth-order accurate. These values were estimated using Equation (5.4), and this is a better approximation when we have more zero crossings. In the case of the scalar field, as the echoing period is not small, obtaining a good approximation is not so easy. Nevertheless, we were still able to find the literature result for Δ. In fact, this is a relevant confirmation of the success of our implementation.

Note that the results obtained using a non-uniform grid are more accurate even with less resolution. This makes sense, since we are able to resolve better the critical phenomena happening around the origin. However, using such grid comes with a downside worth mentioning: when using analytic mesh refinement, one has to take into account the smallest grid spacing in the CFL condition defined in Section 3.8, otherwise we encounter numerical instabilities. This makes the timestep much smaller as we increase resolution.

We now show the profile of some evolutions performed in different regimes. Figure 5.7 shows the rescaled scalar field $\psi(u, x)$ for a subcritical evolution with amplitude A = 0.01 and for a supercritical evolution with A=0.15. Note that the subcritical evolution disperses completely at the end of the evolution.

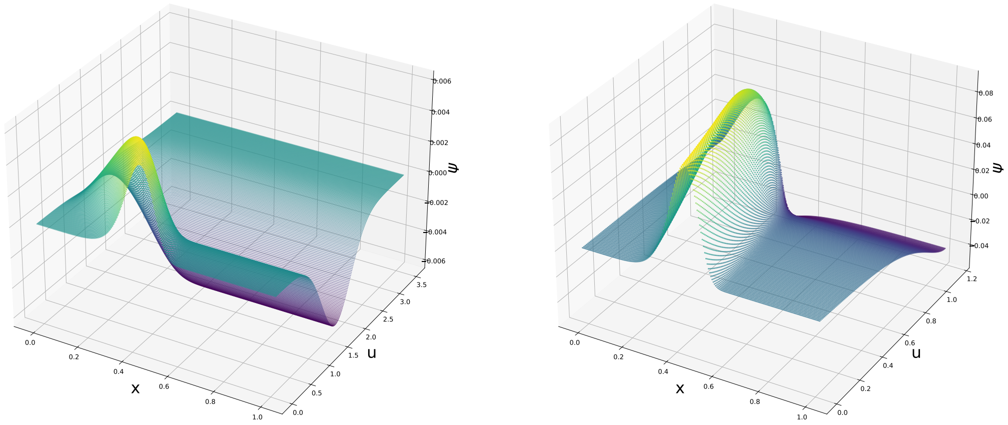

Figure 5.7: Scalar field ψ throughout the evolution. On the left, we plot a subcritical evolution with an initial $A = 0.01$ and on the right we plot a supercritical evolution with $A = 0.15$.

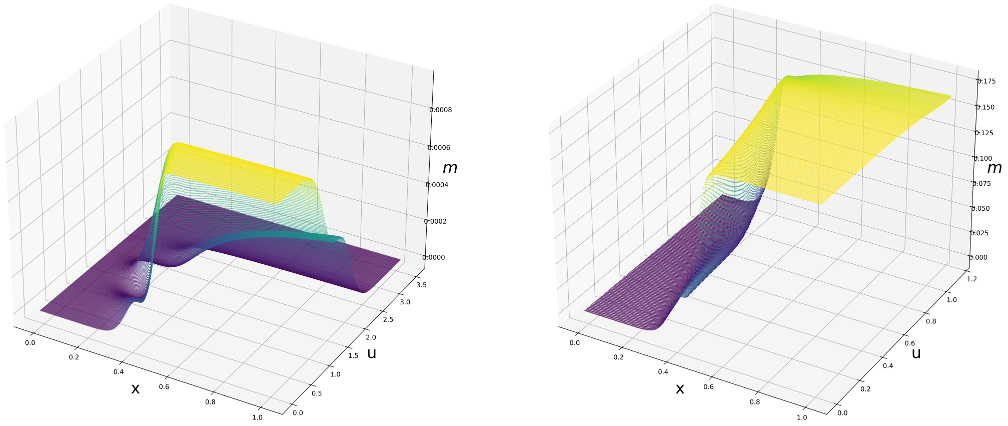

Figure 5.8: Misner-Sharp mass m throughout the evolution. On the left, we plot a subcritical evolution with an initial $A = 0.01$ and on the right we plot a supercritical evolution with $A = 0.15$.

On the other hand, the supercritical evolution stops at earlier times, when an apparent horizon is formed.

Figure 5.8 shows the Misner-Sharp mass $m(u, x)$ for a subcritical evolution with amplitude A = 0.01 and for a supercritical evolution with A=0.15. Similarly to the scalar field plots, the subcritical evolution disperses completely at the end of the evolution. On the other hand, in the supercritical evolution the value of m decays only very slightly.

The rest of this section is organized as follows: first, we study discrete self-similarity of critical solutions, then black hole mass scaling, following an analysis of the Bondi mass decay; lastly, we argue that our results are universal with respect to the initial data.

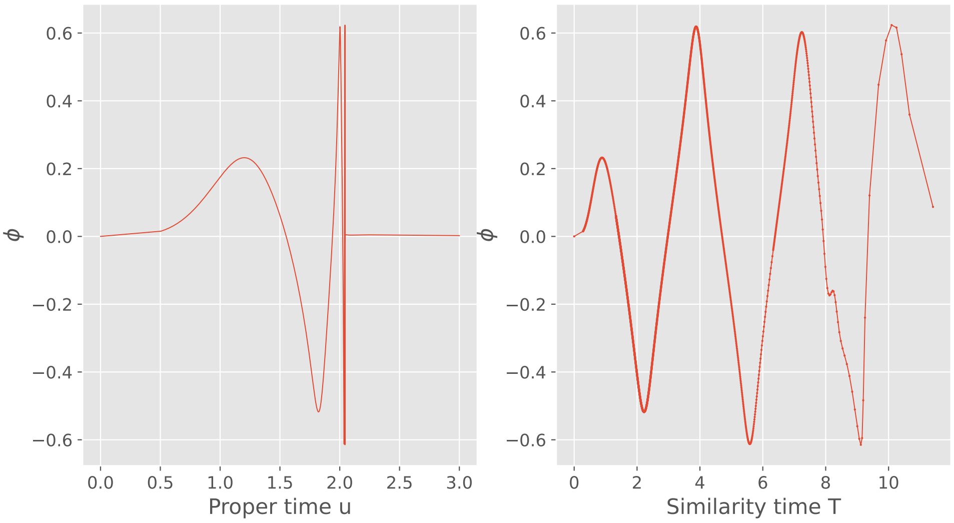

Figure 5.9: Scalar field at the origin as a function of proper time u and adapted time T for a run of N=2×10^5 and global fourth-order accuracy, tuned to 10 decimal places, with $A = 0.12465050165997141$.

5.1.4 DSS Behaviour in Local and Global Quantities

The number of echoes we see depends on the amount of tuning of our solutions, and also of the echoing period Δ. As aforementioned, in the case of a scalar field collapse we have an echoing period of $\Delta \approx 3.4$.

Figure 5.9 shows the value of the scalar field ϕ at the origin, as a function of proper time u, which in our case is the central time, as well as a function of similarity time T. The values of the echoing period Δ in Table 5.1 are extracted from this plot using Equation (5.4).

We see that the scalar field shows discrete self-similarity. We are able to observe almost three complete echoes, in which the third one could be better resolved with more resolution, but this naturally changes the A^*.

In the Appendix A we show other plots obtained for different setups. Figure A.1 shows the preliminary result obtained for a grid with 2000 points and a second-order accurate code. We see that, as expected, using more resolution and higher-order accuracy enables us to resolve more echoes. Figure A.2 shows the most tuned run obtained in a non-uniform grid for $N = 1000$. Table 5.2 shows the parameters obtained in the bisection search in the non-uniform grid used to produce Figure A.2. We see that, in this case, with less points we are able to fine-tune to a higher A^*. However, note that, as mentioned above, using a non-uniform grid makes the evolution slow down considerably as we have to consider the smallest grid-spacing dx in the CFL condition (see Section 3.8). The best result is then the one of Figure 5.9.

Note that the SSH is the past light cone of the accumulation time. Hence, it is the region of spacetime where we expect to observe self-similarity. Moreover, as we're using a characteristic foliation of spacetime, we are able to show that the dynamics of the critical solution, and particularly discrete self-

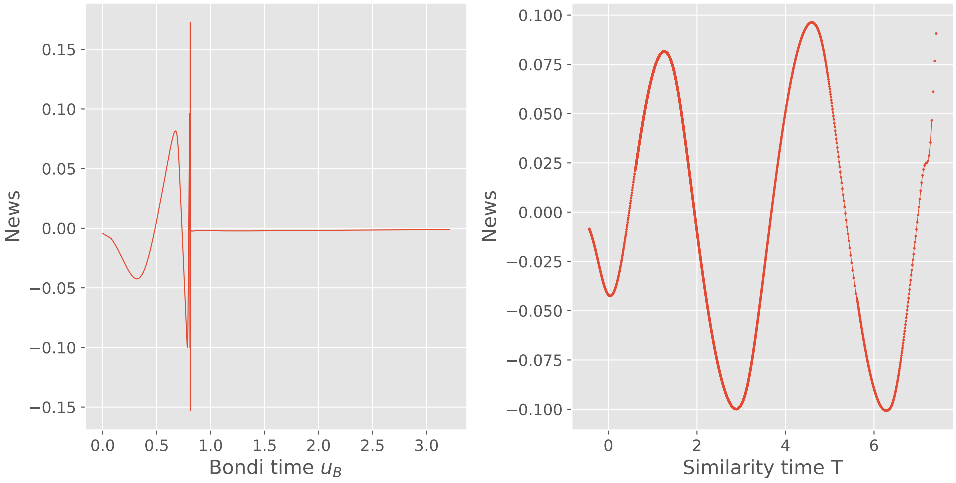

Figure 5.10: News function at future null infinity as a function of Bondi time u_B and adapted time T. The data here presented corresponds to the same run as Figure 5.9.

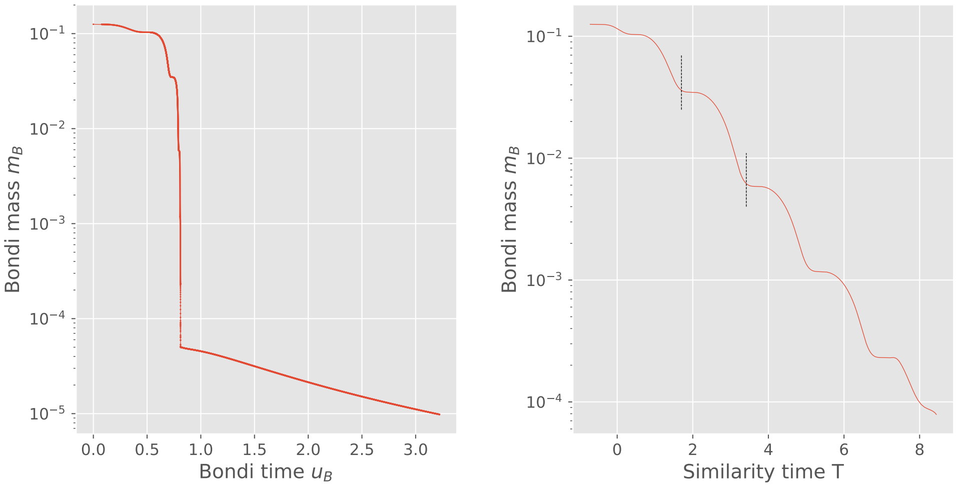

Figure 5.11: Bondi mass as a function of Bondi time u_B and adapted time T. The data here presented corresponds to the same run as Figure 5.9. The vertical lines displayed have a separation of $\Delta/2 = 3.43114040/2$.

similarity, are radiated to an observer at future null infinity $\mathscr{I}^+$. This is shown in Figure 5.10, where we plot the news function. An observer at $\mathscr{I}^+$ is then able to observe features of critical collapse. These features are imprinted also in the Bondi mass, the other radiation quantity discussed in Section 2.3.5.

Figure 5.11 shows the decay in the Bondi mass for a near-critical evolution with initial amplitude $A = 0.124650501659971 41$. We see that the Bondi mass decays exponentially as a function of the similarity time T. On top of this decay, we see that m_B displays a periodic oscillation with period $\Delta/2 = 3.43114040/2$, just like the scalar field does.

Figure 5.12 shows the value of β at future null infinity $\mathscr{I}^+$, as a function of the similarity time T. This is shown for a barely supercritical evolution. As discussed in Section 2.3.5, $H = \beta(u_C, \infty)$ provides a

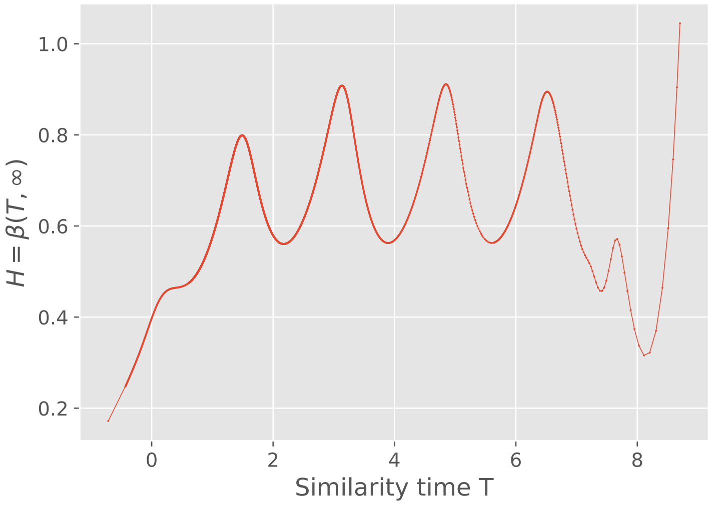

Figure 5.12: Redshift $H = \beta(u_C, \infty)$ for a near supercritical evolution as a function of similarity time T. The data shown corresponds to a run with 2×10^5 points, with A=0.12465050166078954 and tuned to 10 decimal places.

relation between central time and Bondi time through $du_B = 2^{2H} du_C$. We can see that in the case of a large value of H, a finite amount of central time u_C corresponds to an infinite amount of time u_B. This means that light rays being emitted from the centre are infinitely redshifted. Figure 5.12 shows that for $T \approx 8.2$ the redshift diverges, indicating that a black hole is starting to form. Before such formation, the redshift shows discrete self-similarity as the outgoing light rays that approach an observer at $\mathscr{I}^+$ are themselves subject to an oscillating compactness $\frac{2m}{r}$ caused by the near-critical collapse of the scalar field.

Figure 5.13 shows the compactness for a near-critical evolution. With just $N = 2000$, we see that indeed the compactness oscillates for a near-critical evolution, caused by the near-critical collapse of the scalar field.

5.1.5 Black Hole Mass Scaling

As discussed in 2.1, the black hole mass has been found to follow a universal scaling law

$$\ln m_{BH} = \gamma \ln(p - p*) + \text{const.} \tag{5.5}$$

in numerical evolutions of supercritical data. This scaling law has been derived using linear perturbation theory around the critical solution of amplitude A^*.

In this section, we use a uniform grid with $N = 2000$, in a code that is globally fourth-order accurate. Our critical amplitude is $A^* = 0.12465049029170885$ (see Table 5.1), and we perform supercritical runs equally spaced in $\ln(p - p^*)$. The results of such runs are illustrated in Figure 5.14.

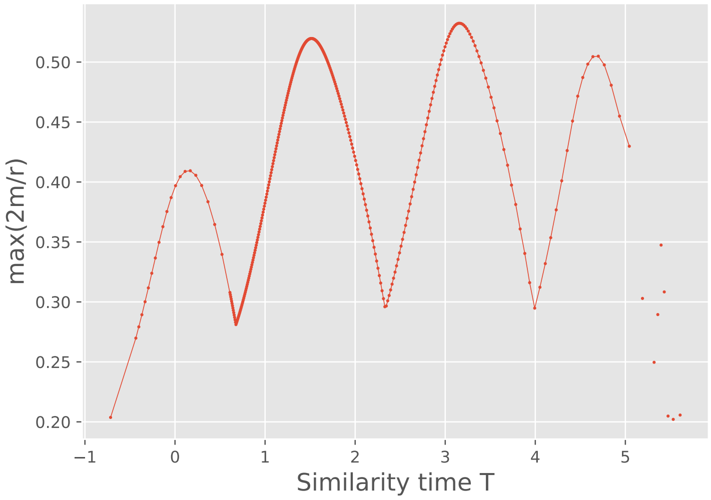

Figure 5.13: Compactness max($\frac{2m}{r}$) for a near-critical evolution as a function of similarity time T. The data shown corresponds to a run with 2000 points, with $A = 0.12465049029170885$ (See Table 5.1).

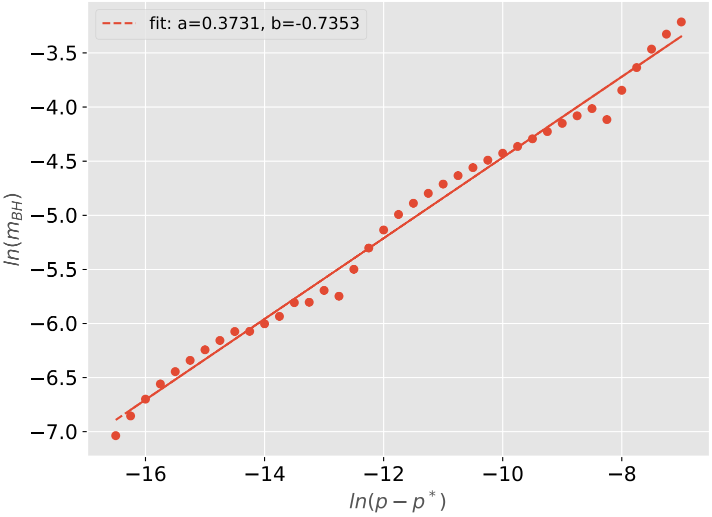

Figure 5.14: Final black hole mass as a function of the distance to the critical parameter p^*. The black hole mass is found to scale as $\ln(m_{BH}) = 0.3731 \ln(p - p*) - 0.7353$. Following from this relation we find a critical exponent of $\gamma = \frac{0.7462}{2} \approx 0.3731$. Each point in this figure corresponds to the final black hole mass of an evolution with 2000 gridpoints, performed in a uniform grid.

For the case of the massless scalar field collapse, numerical simulations and semi-analytical studies have found $\Delta \approx 3.445$ [20]. Perturbation theory arguments have been used to show that $\frac{1}{2}\Delta/\gamma \approx 4.61$ [7], following that $\gamma \approx 0.374$.

In Figure 5.14 we fit our numerical data to find that the black hole mass scales as $\ln(m_{BH}) = 0.3731 \ln(p - p*) - 0.7353$, yielding $\gamma \approx 0.3731$ and $\frac{1}{2}\Delta/\gamma \approx 4.62$, which is very close to the value predicted by theory.

In our numerical simulations, one can estimate the mass of the black hole formed by taking the

Misner-Sharp mass value at the gridpoint and timestep when the compactness $\frac{2m}{r}$ reaches our threshold to mark evolutions as supercritical (see Section 5.1.2). In fact, note that this value gives the mass of the apparent horizon formed, and that this doesn't correspond exactly to the final black hole mass. If the Cosmic Censorship Conjecture holds, there will still be mass-energy left outside of the compactness peak that will eventually fall through the horizon. Nevertheless, the approach we take is still able to reproduce the predicted mass scaling very well, even with just 2000 points.

5.1.6 Bondi Mass Decay

In this Section we aim to explore how Bondi mass behaves in different regimes of initial data. Since the Bondi mass is computed at $\mathscr{I}^+$, we want to have a good resolution in this region. We do this by implementing a grid transformation with more resolution towards the boundaries. We refer to this technique as analytic mesh refinement, as described in Section 3.7. The grid parameters used here are $A = 0.35, k = 0.7, m = 0.5, n = 5$. We use $N = 1000$ points and make use of the globally fourth-order accurate code to produce more reliable results.

Figure 5.15 shows the different possible scenarios. In the supercritical regime, the evolution naturally stops once the compactness is above the criteria explained in Section 5.1.2, and an apparent horizon forms. On the other hand, for a very subcritical evolution the Bondi mass decays very rapidly. As we get near the critical amplitude, the Bondi mass decay at late times is found to describe a power-law. We fit this decay and find that the exponent is ≈ 2.43. Note that this decay is dependent of the initial data, and that's the reason why our exponent ≈ -2.43 differs from the exponent ≈ -5.06 found in [7].

In order to validate our results, we now aim to compare the values of the Bondi mass when computed with our numerical scheme with the values calculated from an analytical expression obtained from the Einstein equations that we don't solve directly in our scheme.

Using the expression given by Equation (2.38), we plot the mass loss $\partial_u(m_B)$ at future null infinity throughout the evolution. In Figure 5.16, we plot the numerical results obtained by taking a time derivative of the variable m, which is solved at each null slice by integrating out a hypersurface equation. We see that these values correspond almost exactly to the analytical expected result calculated using Equation (2.38).

Note that this is a non-trivial test to our numerical scheme, since we don't directly solve all of Einstein's equations, and in particular we don't solve Equation (2.36). Instead, we calculate m in slices of constant u by integrating out an expression that depends on β and ψ (Equation (2.18)).

This gives more supporting evidence of the validity of our results and of a successful implementation.

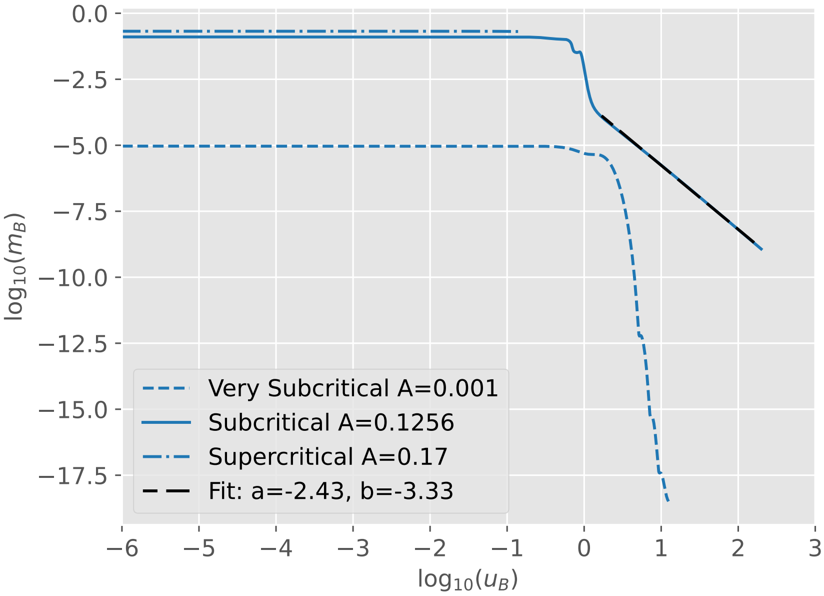

Figure 5.15: Comparing Bondi mass decay for initial data that is very subcritical (A=0.001), subcritical (A=0.1256) and supercritical (A=0.17). In the subcritical case, the Bondi mass is found to decay for late times with a power-law exponent of -2.43.

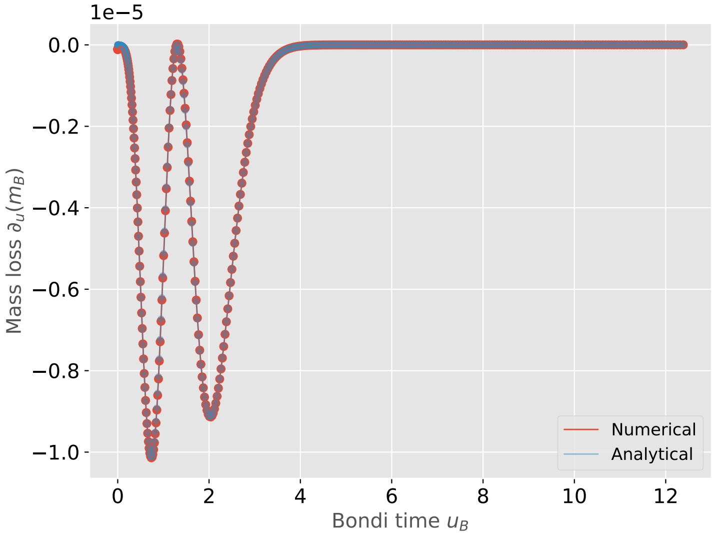

Figure 5.16: We compare the mass loss at future null infinity $\mathscr{I}^+$. The numerical values refer to the values obtained by taking a time derivative of m solved throughout our evolution. The analytical value refers to the values computed using a derived equation for the mass loss at $\mathscr{I}^+$.

5.1.7 Universality

All results presented so far consider the same initial data described by Equation (5.1), with $\sigma = 0.3$ and $r_0 = 0.7$. We have tuned one-parameter families by changing the amplitude A, and investigated different grid resolutions. We now study the collapse of different families of initial data, particularly by considering

Table 5.3: Critical parameters obtained for different families of initial data, with a uniform grid of 2000 points, using a code that is globally fourth-order accurate. We vary the value of σ and keep $r_0 = 0.7$. A^* denotes the critical amplitude, fine-tuned up to 11 decimal places, u^* denotes the accumulation time and Δ is the self-similarity echoing period defined in Section 2.1.2.

σ	A^*	u^*	Δ
0.1	0.046334778655545986	1.5608430946600613	3.56772728
0.2	0.08974216673803313	1.7841975845723363	3.45251302
0.4	0.14985093340204908	2.322949721065589	3.38035981
0.5	0.16671677902267223	2.6082639947157817	3.42612611
0.6	0.17724439699825775	2.9003615008040065	3.52804766

initial data of different σ and tuning to the parameter A. The results of such runs are presented in Table 5.3.

We note that the value of Δ deviated slightly from the value calculated in Section 5.1.2, as we have only tuned to 11 decimal places and used less resolution for these runs. Because there are less zero crossings of the scalar field ϕ, the approximation given by Equation (5.4) is less reliable.

As expected, using an initial pulse that is narrower corresponds to a smaller accumulation time, meaning that the apparent horizon starts to form at earlier times in the evolution. Additionally, the critical amplitude is smaller for lower values of σ.

We are able to obtain the same critical phenomena picture as before (compare Figure 5.9 with Figure 5.17), despite the fact that here we use different initial data ($\sigma = 0.5$ in contrast to $\sigma = 0.3$ in the previous sections). This indicates that no matter the profile of the initial data, a near-critical solution will lose its features along the evolution and approach the critical solution, exhibiting the characteristic echoes, even for a resolution of just 2000 points.

We now aim to calculate the critical exponent γ, as done previously in Section 5.1.5. We fix $\sigma = 0.4$ and we find the value of the critical amplitude to be 0.14985093340204908, after doing the usual bisection search (see Table 5.3). We perform supercritical runs that are evenly spaced in $\ln(p - p^*)$ and again estimate the black hole mass by reading the Misner-Sharp mass at the gridpoint where the compactness reaches our apparent horizon formation criterion of $\frac{2m}{r} > 0.6$. Figure 5.18 demonstrates the results of such runs.

From Figure 5.18 we are able to extract an exponent $\gamma \approx 0.3765$, which is approximately the same as the one obtained in Section 5.1.5, despite here using different initial data. We hence show that there's universality, as all near-critical evolutions look the same as they approach the critical solution.

5.2 Yang-Mills Field Collapse

The implementation of a Yang-Mills field collapse is more subtle than a scalar field one. This is due to the fact that the wave equation for a Yang-Mills field has now a source term of the form $-\frac{W(1-W^2)}{r^2}$ (see

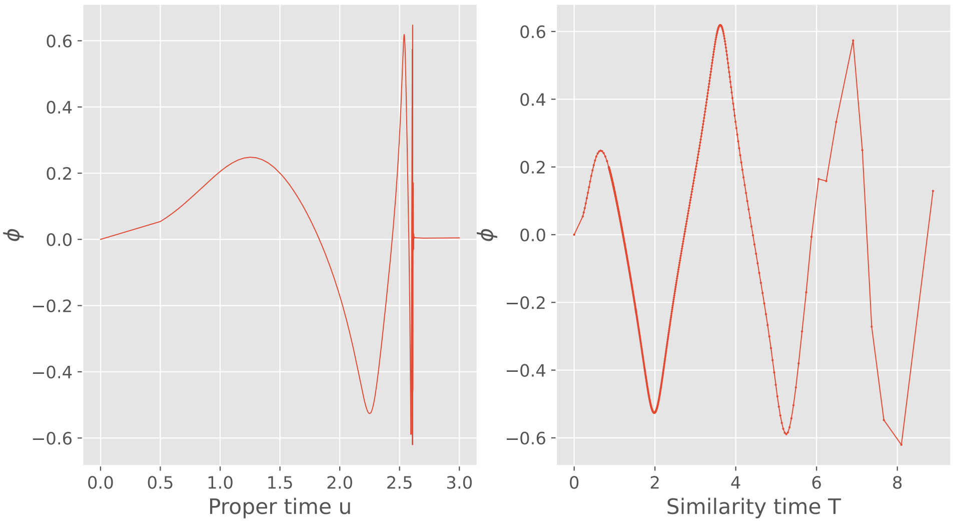

Figure 5.17: Scalar field at the origin as a function of similarity time T and adapted time T. The results shown correspond to a run with $\sigma = 0.5$, and $N = 2000$ points in a uniform grid, tuned to 11 decimal places in $A^* = 0.16671677902267223$. Although the initial data in this picture differs from previous sections, we are able to obtain the same critical phenomena picture as before (see Figure 5.9).

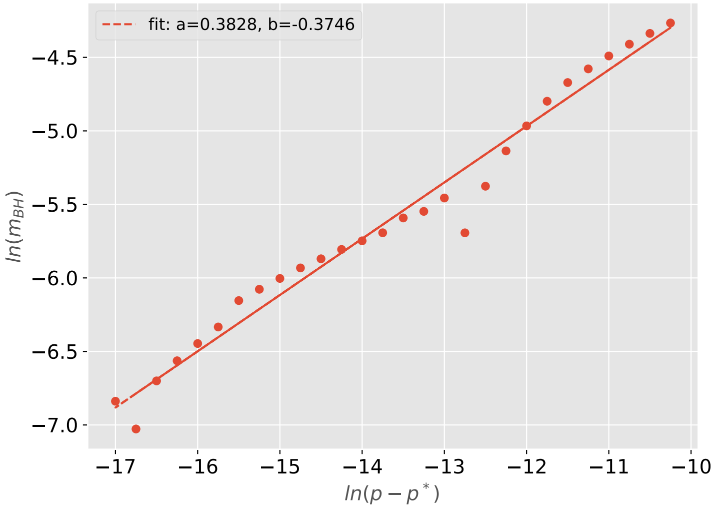

Figure 5.18: Final black hole mass as a function of the distance to the critical parameter p^*. The black hole mass is found to scale as $\ln(m_{BH}) = 0.3765 \ln(p - p*) - 0.4414$. Following from this relation we find a critical exponent of $\gamma \approx 0.3765$. Each point in this figure corresponds to the final black hole mass of an evolution with 2000 gridpoints, performed in a uniform grid.

Equation (2.31)). We then have to choose an appropriate parametrization for W such that we regularize our equations both at the origin and at $\mathscr{I}^+$.

We start by implementing two toy models for the Yang-Mills collapse. We then implement the collapse in full GR, extracting preliminary critical collapse analysis.

5.2.1 Yang-Mills Toy Models

The wave equation for the Yang-Mills field in $2D$ is given by Equation (2.31). Let us consider as a first toy model the case in which we have no source term in the Yang-Mills wave equation. We can write this as

$$\Box_h W = e^{-2\beta}\left[\left(\frac{V}{r}\right)_{,r}\partial_r - 2\partial_u\partial_r + \frac{V}{r}\partial_{rr}\right]W = 0, \tag{5.6}$$

which in flat spacetime ($m = \beta = 0$, $V/r = 1$) corresponds to

$$\Box_h W = \left[-2\partial_u\partial_r + \partial_{rr}\right]W = 0. \tag{5.7}$$

Since we are not considering the non-linearity of the Yang-Mills field, W simply obeys the wave equation with no source. In this case, the ansatz for W can be written as the sum of an outgoing and an ingoing wave

$$W(u,r) = f(u) + g(u+2r). \tag{5.8}$$

At the centre we want to have $W(u) = 1$ which implies that $f(u) + g(u) = 1$. The solution for W can be written as $W(u,r) = 1 - g(u) + g(u+2r)$. We expand this solution around the origin in powers of r, and find that the correct ansatz for W in this case is $W = 1 + \mathcal{O}(r)$. We then make the substitution $W(u,r) = 1 + x\chi(u,r)$ in Equation (5.6) and find the following evolution equation

$$((x\chi)_{,u})_{,r} = \frac{1}{2}(x\chi)_{,rr}. \tag{5.9}$$

Our evolution variables are then $x\chi$ and $(x\chi)_{,u}$. At fixed u, we solve for $(x\chi)_{,u}$ by integrating out Equation (5.9) and then find $x\chi$ in the next slice. The initial data for $x\chi(u,r)$ is set as

$$x\chi(u,r) = Ax\exp(-\left((x-r_0)/\sigma\right)^2) + Ax\exp(-\left((x+r_0)/\sigma\right)^2), \tag{5.10}$$

with $A = 0.12$, $\sigma = 0.07$ and $r_0 = 0.3$. This choice of initial data satisfies $W = 1 + \mathcal{O}(r)$ around the origin. Instead of working in a radial coordinate, we use instead a compactified one and resort ourselves to lopsided finite differences operators. In this way, we avoid the need for boundary conditions at the outer boundary, as our calculations are performed only with points that belong to our domain and are being evolved.

Figure 5.19 shows the norm convergence result obtained for this first toy model. Note that increasing resolution leads to a better convergence.

We now want to study the case in which we include a source term in the Yang-Mills have equation, which can be written as

$$\Box_h W = \left[-2\partial_u\partial_r + \partial_{rr}\right]W = \frac{-W(1-W^2)}{r^2}. \tag{5.11}$$

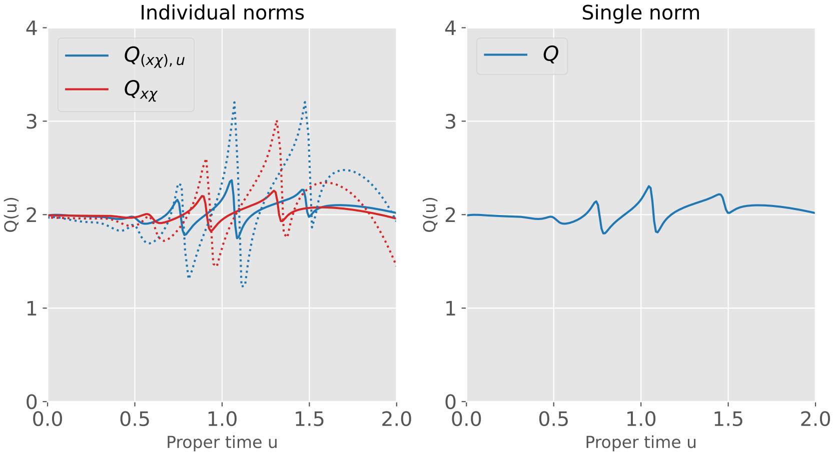

Figure 5.19: Convergence factor Q(t) throughout the evolution for the first Yang-Mills toy model, using a code that is globally second-order accurate. The dotted lines correspond to a grid with 100 points and the solid lines correspond to a grid with 200 points. On the left, we show Q(t) for each evolution variable individually, and on the right we show the norm of all the variables together. The dotted lines correspond to a grid with 100 points and the solid lines correspond to a grid with 200 points. We can see that as we increase resolution the convergence factor Q gets closer to 2, both for each field individually as for the single norm. An initial pulse of amplitude $A = 0.01$ was considered.

In this case, solutions for W have to be of the form $W = 1 + x^2\chi$, since we pick the ground-state $W = 1$ and $\chi = \mathcal{O}(1)$ both at the origin and at $\mathscr{I}^+$. Using this ansatz in Equation (5.11), we find the following evolution equation

$$((x^2\chi)_{,u})_{,r} = -\frac{(1-x)^2x^2\chi}{x^2} - \frac{3(1-x)^2x^2\chi^2}{2x^2} - \frac{(1-x)^2x^2\chi^3}{2x^2} + \frac{1}{2}(x^2\chi)_{,rr}. \tag{5.12}$$

Our evolution variables are then $x^2\chi$ and $(x^2\chi)_{,u}$. At fixed u, we solve for $(x^2\chi)_{,u}$ by integrating out Equation (5.12) and then find $x^2\chi$ in the next slice. The initial data for $(x^2\chi)$ is set as

$$x^2\chi(u_0, r) = Ax^2\exp(-((x-r_0)/\sigma)^2) + Ax^2\exp(-((x+r_0)/\sigma)^2), \tag{5.13}$$

with $A = 0.01$, $\sigma = 0.07$ and $r_0 = 0.3$, which again satisfies $W = 1 + x^2\chi$.

Figure 5.20 shows the norm convergence result obtained for the second toy model. As in the first toy model studied, increasing resolution leads to a better convergence both in each variable individually as in the single norm. The overall convergence result in noticeably better in this second case.

The implementation of these two toy models serves as a starting point in order to study the case of the Yang-Mills field collapse in full GR. We recall that including a Yang-Mills field is not trivial as the wave equation for this field has a non-linear term which doesn't appear in the scalar field scenario.

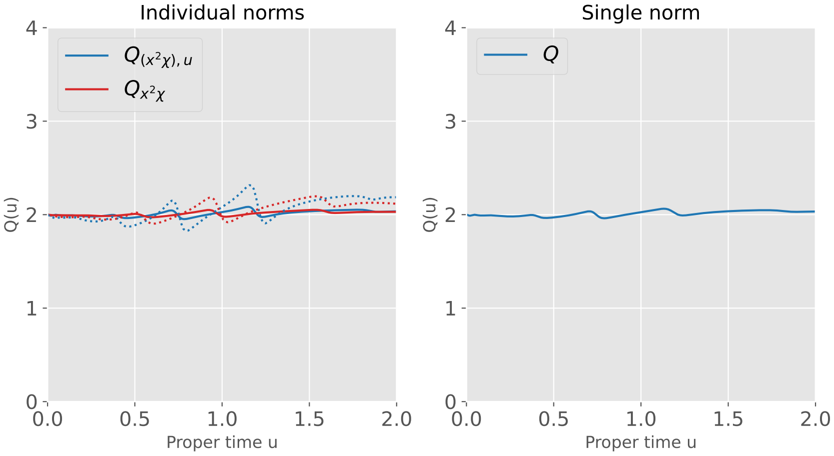

Figure 5.20: Convergence factor Q(t) throughout the evolution for the second Yang-Mills toy model, using a code that is globally second-order accurate. The dotted lines correspond to a grid with 100 points and the solid lines correspond to a grid with 200 points. On the left, we show Q(t) for each evolution variable individually, and on the right we show the norm of all the variables together. An initial pulse of amplitude $A = 0.01$ was considered.

5.2.2 Convergence Tests

In Section 3.3 we propose an evolution scheme for the collapse of a Yang-Mills field, which we now implement.

Recall from Section 2.3.3 that $W(u,r) = 1 + x^2\chi \equiv 1 + \xi(u,r)$ and $\xi(u,r) = \mathcal{O}(2)$. We choose initial data for ξ as:

$$\xi(u_0, x) = Ar(x)^2 \exp\left[-\left(\frac{r(x) - r_0}{\sigma}\right)^2\right], \tag{5.14}$$

in which we use $A = 0.01$, $r_0 = 0.3$ and $\sigma = 0.1$ for the convergence tests.

Figure 5.21 shows the convergence factor calculated throughout the evolution for a code that is globally second-order accurate. The dotted lines correspond to a grid with 100 points and the solid lines correspond to a grid with 200 points. We can see that as we increase resolution the convergence factor Q gets closer to 2, both for each field individually as for the single norm. As in the scalar field collapse, these results not only reassure us that our code is globally second-order accurate, but also that this result is better as we increase resolution. We stop the convergence test when the magnitude of all fields is smaller than 10^{-7}.

5.2.3 Identification of Critical Behaviour

In this section, we analyse different evolution regimes of a Yang-Mills field collapse. As we did previously in Section 5.1.2, we monitor the compactness $\frac{2m}{r}$ throughout the evolution, marking runs as supercritical when the criterion $\frac{2m}{r} > 0.7$ is met. As before, our timestep is adaptive in order to meet the CFL-stability

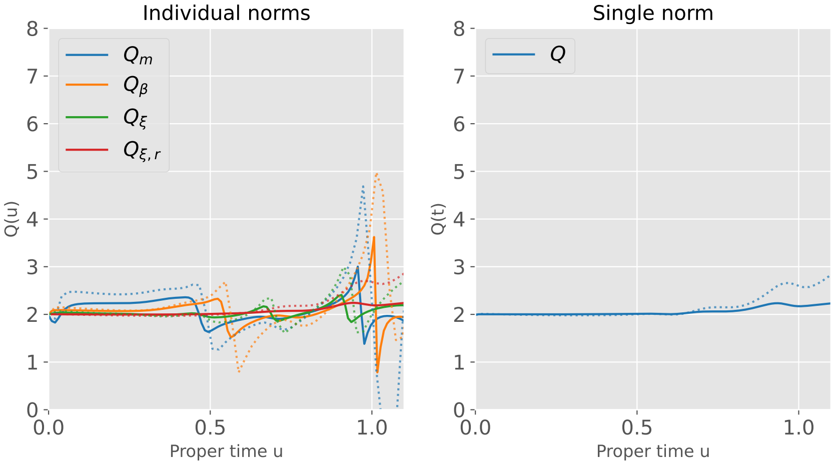

Figure 5.21: Convergence factor Q(t) throughout the evolution for a uniform grid, using a code that is globally second-order accurate. The dotted lines correspond to a grid with 100 points and the solid lines correspond to a grid with 200 points. On the left, we show Q(t) for each evolution variable individually, and on the right we show the norm of all the variables together.

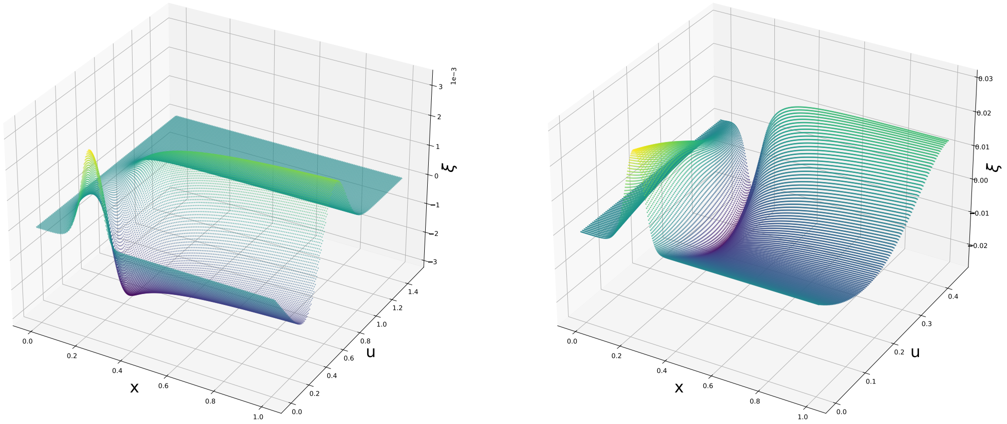

Figure 5.22: $\xi = W - 1$ throughout the evolution. On the left, we plot a subcritical evolution with an initial $A = 0.01$ and on the right we plot a supercritical evolution with $A = 0.092$ for $N = 400$.

condition given by Equation (3.21).

Figure 5.22 shows the value of our evolution variable ξ as a function of u and x for both subcritical and supercritical initial data. Recall from Section 2.3.3 that $\xi \equiv W - 1$. We see that, as expected, ξ remains 0 at the origin and disperses completely at the end of the subcritical evolution. The supercritical evolution naturally stops at an earlier time, when our compactness criterion is met.

Figure 5.23 shows the value of m as a function of u and x. We see that, as before, m disperses completely at the end of the subcritical evolution.

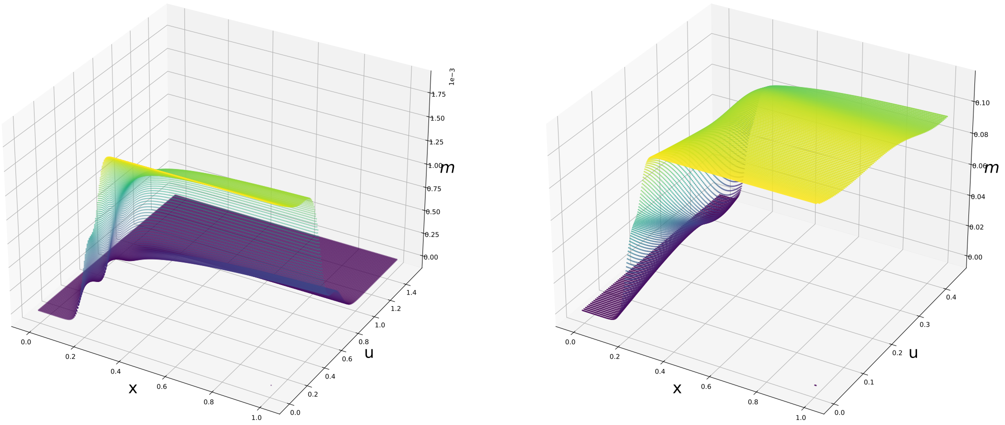

Figure 5.23: Misner-Sharp mass m throughout the evolution. On the left, we plot a subcritical evolution with an initial $A = 0.01$ and on the right we plot a supercritical evolution with $A = 0.092$ for $N = 400$.

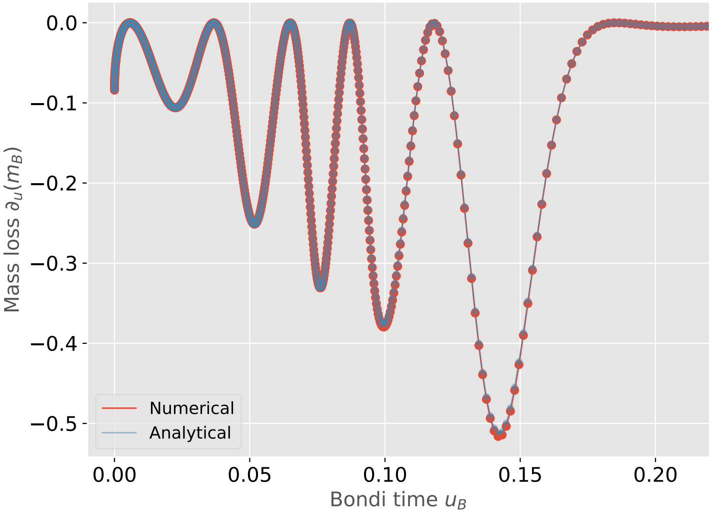

Figure 5.24: We compare the mass loss at future null infinity $\mathscr{I}^+$ for the Yang-Mills collapse code. The numerical values refer to the values obtained by taking a time derivative of m solved throughout our evolution. The analytical value refers to the values computed using a derived equation for the mass loss at $\mathscr{I}^+$.

5.2.4 Bondi Mass Decay

As studied in Section 5.1.6 for the scalar field collapse, we now want to test our implementation by comparing the values of the Bondi mass when computed with the numerical scheme with the values calculated from an analytical expression obtained from the EFE that we don't solve directly in our evolution.

Equation (2.40) gives an expression for the mass loss $\partial_u(m_B)$ at future null infinity throughout the evolution. In Figure 5.24, we plot the numerical results obtained by taking a time derivative of the variable m, which is solved at each null slice by integrating out a hypersurface equation. We see that these values

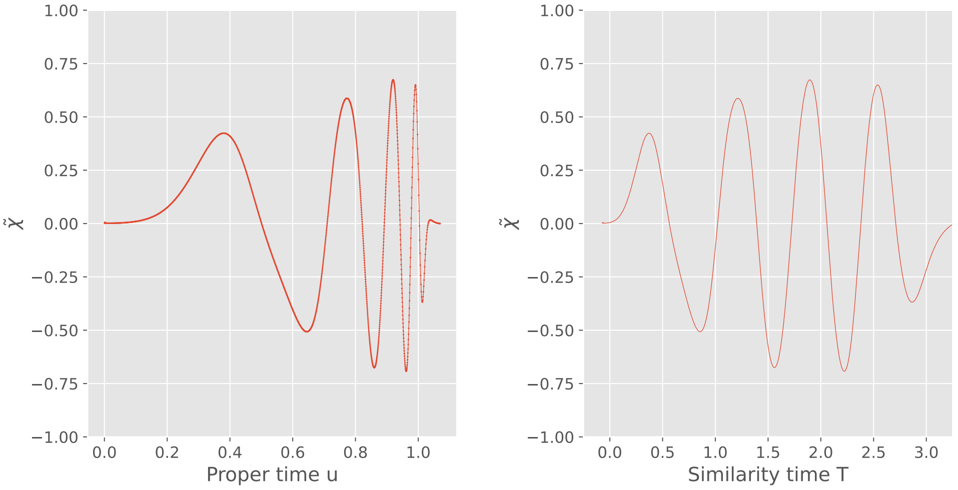

Figure 5.25: $\tilde{\chi}$ at the origin as a function of proper time u and adapted time T for a run of N=2000 and global second-order accuracy, tuned to 6 decimal places, with $A = 0.0886421$.

correspond almost exactly to the analytical expected result calculated using Equation (2.40). The values shown correspond to a subcritical evolution with $N = 1000$ and $A = 0.08859375$.

As in the scalar field case, this is a non-trivial test to our numerical scheme, since we don't directly solve all Einstein equations, and in particular we don't solve Equation (2.40). This gives more supporting evidence of the validity of our results and of a successful implementation.

5.2.5 Preliminary Study of DSS Behaviour in Local Quantities

Similarly to the study provided in Section 5.1.4, we now look to investigate how local quantities such as χ behave in evolutions that approach the critical solution. Recall from Section 2.3.3 that $W = 1 + x^2\chi \equiv 1 + \xi$. Following the work of Gundlach, et al. [8], we note that χ is not compatible with exact DSS. However, the critical solution observed should be of the form

$$\tilde{\chi} = e^{-T}\chi, \tag{5.15}$$

where T is the similarity time, which is periodic in Δ.

We perform a bisection search with $N = 2000$ points and find a critical amplitude of $A^* \approx 0.0886421$, tuned to 6 decimal places. Figure 5.25 shows the value of $\tilde{\chi}$ at the origin as a function of proper time u and of similarity time T for an evolution with $A^* = 0.0886421$. We see that indeed $\tilde{\chi}$ is DSS with an echoing period of $\Delta \approx 0.662415$, estimated using Equation (5.4). Note that we are able to show that the solution is DSS using much less resolution and tuning than in the scalar field collapse. This is because for the scalar field we have an echoing period of $\Delta \approx 3.44$ and in the Yang-Mills field $\Delta \approx 0.6$ [4]. Obtaining a better estimation of Δ would be possible with more tuning, as the approximation given by

Equation (5.4) becomes more reliable. This would also allow us to see more echoes. Nevertheless, the ones we observe show approximately the same amplitude as the literature results [8].

Lastly, we recall that the code implemented for the Yang-Mills field collapse shows good numerical convergence, as seen in Figure 5.21. Additionally, the results from Section 5.2.4 give supporting evidence of a successful implementation. As future work, we intend to further tune to the critical parameter A^* and observe more echoes, extracting additional critical phenomena analysis. Nevertheless, our results already provide a satisfactory picture of the critical collapse of a Yang-Mills field.

6

Conclusions

Contents

6.1 Conclusions 67
6.2 Future Work 68

6.1 Conclusions

The present thesis provides a numerical study of critical gravitational collapse in GR. The collapse of a scalar field in spherical symmetry was thoroughly analysed.

The aim of the work was to study critical phenomena from the point of view of an observer located at future null infinity $\mathscr{I}^+$. We considered a null foliation of spacetime and solved a CIVP. We also included both the origin and future null infinity in our grid through the compactification of our radial domain. This setup allowed us to compute radiation quantities at $\mathscr{I}^+$ such as the Bondi Mass and the news function. This is relevant as we can mimic what a detector of gravitational waves would observe in the advent of critical phenomena.

Near-critical evolutions were shown to exhibit features of the critical solution, such as reproducing themselves in echoes of echoing period $\Delta \approx 3.4$. In supercritical evolutions the mass of the final black hole was shown to scale as a power-law in relation to the distance in parameter space to the critical parameter. The critical exponent of such scaling was found to be $\gamma \approx 0.37$. We also argue that there is universality in critical gravitational collapse: we investigated the collapse of different families of initial data and were able to extract the same parameters and the critical solution exhibited the same shape in the late stages of the evolution.

What is interesting about our approach is that we were able to show that features of critical collapse radiate to future null infinity. Particularly, the Bondi mass and the news function show self-similar dynamics. This is also the case with the redshift, due to the fact that outgoing light rays are subject to an oscillating compactness as radiation approaches $\mathscr{I}^+$.

Our numerical approach differs from previous works as we constructed a code that is globally fourth-order accurate. This code produces better results than the second-order accurate code we construct, although we found that obtaining clean convergence for second-order accurate methods is more straightforward. On the other hand, obtaining clean convergence in higher-order schemes in null slicing is still an open problem which we try to tackle by considering different approaches. Note that using a foliation of spacetime based on Cauchy or hyperboloidal surfaces would resolve this problem as it is more straightforward to understand the parity of the functions in that case.

In the end, finding good fourth-order convergence took more time than initially expected. The approach that ended up producing best convergence results is to consider a non uniform grid which has more resolution towards the boundaries of our domain. The downside of such approach is that evolutions are slowed down considerably in order to avoid CFL instabilities. We also consider a different integration scheme than the work of Pürrer, et al. [7] which has the advantage of being more general and easily reused.

Lastly, we presented in this work two toy models of a Yang-Mills collapse, as well as preliminary results of a full GR Yang-Mills field critical collapse. As discussed, the non-linearity of this field makes the implementation more subtle than in the scalar field case. Both the toy models employed, as well as the full Yang-Mills field collapse show good numerical convergence. We testify the existence of critical behaviour and are able to extract an echoing period of $\Delta \approx 0.662415$.

6.2 Future Work

Having successfully studied the critical collapse of a scalar field and observed preliminary DSS behaviour of a Yang-Mills field collapse, further tuning to the critical solution in this second physical model is a future work. We hope that this will culminate in the publication of a paper in an international peer-reviewed journal.

To our knowledge, such critical collapse hasn't been studied for a null slicing of spacetime with compactified radial domain. The code implemented in Section 5.2.3, which shows good convergence, will be used to extract further critical phenomena analysis, as done in the scalar field case.

Lastly, critical collapse studies require high numerical precision in order to fine-tune our solutions. In general, this is often a challenge which one can mitigate by implementing codes with higher accuracy schemes and the use of quad precision should be further investigated.

Bibliography

[1] M. Pürrer, “Global versus local aspects of critical collapse,” Ph.D. dissertation, Wien University, 2007.

[2] A. V. Frolov, “Continuous self-similarity breaking in critical collapse,” *Physical Review D*, vol. 61, no. 8, mar 2000. [Online]. Available: https://doi.org/10.1103%2Fphysrevd.61.084006

[3] C. Gundlach and J. M. Martín-García, “Critical phenomena in gravitational collapse,” *Living Reviews in Relativity*, vol. 10, no. 1, dec 2007. [Online]. Available: https://doi.org/10.12942%2Flrr-2007-5

[4] T. W. Baumgarte, C. Gundlach, and D. Hilditch, “Critical phenomena in the gravitational collapse of electromagnetic waves,” *Phys. Rev. Lett.*, vol. 123, p. 171103, Oct 2019. [Online]. Available: https://link.aps.org/doi/10.1103/PhysRevLett.123.171103

[5] A. V. Astashenok, K. Mosani, S. D. Odintsov, and G. C. Samanta, “Gravitational collapse in general relativity and in r2-gravity: A comparative study,” *International Journal of Geometric Methods in Modern Physics*, vol. 16, no. 03, p. 1950035, mar 2019. [Online]. Available: https://doi.org/10.1142%2Fs021988781950035x

[6] M. W. Choptuik, “Universality and scaling in gravitational collapse of a massless scalar field,” *Phys. Rev. Lett.*, vol. 70, pp. 9–12, Jan 1993. [Online]. Available: https://link.aps.org/doi/10.1103/PhysRevLett.70.9

[7] M. Pürrer, S. Husa, and P. C. Aichelburg, “News from critical collapse: Bondi mass, tails, and quasinormal modes,” *Physical Review D*, vol. 71, no. 10, may 2005. [Online]. Available: https://doi.org/10.1103%2Fphysrevd.71.104005

[8] C. Gundlach, T. W. Baumgarte, and D. Hilditch, “Critical phenomena in gravitational collapse with two competing massless matter fields,” *Physical Review D*, vol. 100, no. 10, nov 2019. [Online]. Available: https://doi.org/10.1103%2Fphysrevd.100.104010

[9] E. Poisson, *A Relativist’s Toolkit: The Mathematics of Black-Hole Mechanics*. Cambridge University Press, 12 2009.

[10] R. Gómez and J. Winicour, “Asymptotics of gravitational collapse of scalar waves.” *Journal of Mathematical Physics*, vol. 33, no. 4, pp. 1445–1457, Apr. 1992.

[11] O. Rinne, “An axisymmetric evolution code for the einstein equations on hyperboloidal slices,” *Classical and Quantum Gravity*, vol. 27, no. 3, p. 035014, jan 2010. [Online]. Available: https://doi.org/10.1088%2F0264-9381%2F27%2F3%2F035014

[12] ——, “Formation and decay of einstein-yang-mills black holes,” *Physical Review D*, vol. 90, no. 12, dec 2014. [Online]. Available: https://doi.org/10.1103%2Fphysrevd.90.124084

[13] M. Maliborski and O. Rinne, “Critical phenomena in the general spherically symmetric einstein-yang-mills system,” *Physical Review D*, vol. 97, no. 4, feb 2018. [Online]. Available: https://doi.org/10.1103%2Fphysrevd.97.044053

[14] M. Pürrer and P. C. Aichelburg, “Tails for the einstein–yang–mills system,” *Classical and Quantum Gravity*, vol. 26, no. 3, p. 035004, jan 2009. [Online]. Available: https://doi.org/10.1088%2F0264-9381%2F26%2F3%2F035004

[15] H. Friedrich and A. D. Rendall, “The cauchy problem for the einstein equations,” *Lect. Notes Phys.*, 2000. [Online]. Available: https://arxiv.org/abs/gr-qc/0002074

[16] A. D. Rendall, “Reduction of the characteristic initial value problem to the cauchy problem and its applications to the einstein equations,” *Proceedings of the Royal Society of London. Series A, Mathematical and Physical Sciences*, vol. 427, no. 1872, pp. 221–239, 1990. [Online]. Available: http://www.jstor.org/stable/51794

[17] F. Pretorius, “Numerical simulations of gravitational collapse,” Ph.D. dissertation, The University of British Columbia, 2002.

[18] M. Alcubierre, “Introduction to 3+1 numerical relativity,” *Introduction to 3+1 Numerical Relativity*, 04 2006.

[19] H.-O. Kreiss and J. Oliger, *Stability and Convergence for Difference Methods*. John Wiley & Sons, Ltd, 2013, ch. 4, pp. 109–152. [Online]. Available: https://onlinelibrary.wiley.com/doi/abs/10.1002/9781118548448.ch4

[20] E. Jiménez-Vázquez and M. Alcubierre, “Critical gravitational collapse of a massive complex scalar field,” *Physical Review D*, vol. 106, no. 4, aug 2022. [Online]. Available: https://doi.org/10.1103%2Fphysrevd.106.044071

[21] T. W. Baumgarte, “Aspherical deformations of the choptuik spacetime,” *Physical Review D*, vol. 98, no. 8, oct 2018. [Online]. Available: https://doi.org/10.1103%2Fphysrevd.98.084012

A

DSS Behaviour Results

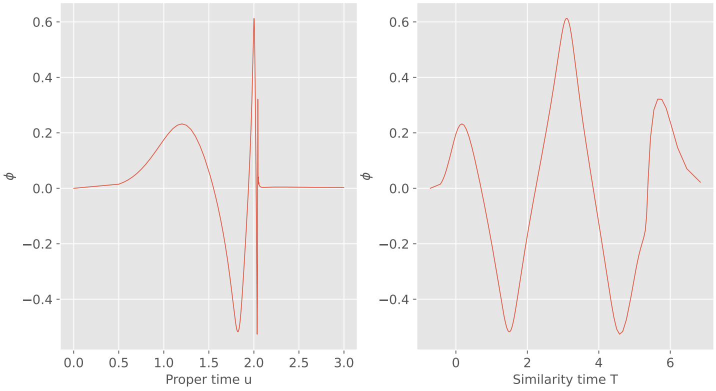

Figure A.1: Scalar field at the origin as a function of proper time u and adapted time T for a preliminary run of N=2000 and global second-order accuracy.

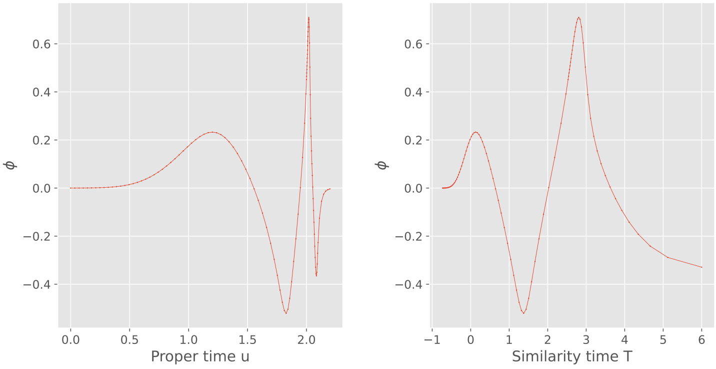

Figure A.2: Scalar field at the origin as a function of proper time u and adapted time T in a non uniform grid of $N = 1000$ points. The grid parameters used are $\Theta = 0.44$, $n = 4.0$, $k = 0.47$, $m = 0.5$. The critical parameter is $A^{*} = 0.12491048189863257$, tuned to 10 decimal places.